

1
2 **Effects of topographic and meteorological parameters**
3 **on the surface area loss of ice aprons in the Mont-Blanc massif (European Alps)**
4

5 Suvrat Kaushik ^{1,2}, Ludovic Ravanel^{1,3}, Florence Magnin¹, Yajing Yan², Emmanuel Trouve², Di-
6 ego Cusicanqui⁴
7

8 ¹ EDYTEM, Univ. Savoie Mont-Blanc, Univ. Grenoble Alpes, CNRS, 73000 Chambéry, France

9 ² LISTIC, Univ. Savoie Mont Blanc, Polytech, F-74944 Annecy-le-Vieux, France

10 ³ Department of Geosciences, University of Oslo, Sem Sælands vei 1, 0371 Oslo, Norway

11 ⁴ IGE, Univ. Grenoble Alpes - CNRS, F-38000 Grenoble, France

12 **Correspondence:** Suvrat Kaushik (suvrat.kaushik@univ-smb.fr)
13
14

15 **Abstract**

16 Ice aprons (IAs) are part of the critical components of the Alpine cryosphere. As a result of the
17 changing climate over the past few decades, deglaciation has resulted in a surface decrease of IAs,
18 which has not yet been documented, except for a few specific examples. In this study, we quantify
19 the effects of climate change on IAs since the mid-20th century in the Mont-Blanc massif (western
20 European Alps). We then evaluate the role of meteorological parameters and the local topography
21 in the behaviour of IAs. We precisely mapped the surface areas of 200 IAs using high-resolution
22 aerial and satellite photographs from 1952, 2001, 2012 and 2019. From the latter inventory, the
23 surface area of the present individual IAs ranges from 0.001 to 0.04 km². IAs have lost their surface
24 area over the past 70 years, with an alarming increase since the early 2000s. The total area, from
25 7.93 km² in 1952, was reduced to 5.91 km² in 2001 (-25.5 %) before collapsing to 4.21 km² in
26 2019 (-47 % since 1952). We performed a regression analysis using temperature and precipitation
27 proxies to understand better the effects of meteorological parameters on IA surface area variations.
28 We found a strong correlation between both proxies and the relative area loss of IAs, indicating
29 the significant influence of the changing climate on the evolution of IAs. We also evaluated the

role of the local topographic factors in the IAs area loss. At a regional scale, factors like direct solar radiation and elevation have an important influence on the behaviour of IAs, while others like curvature, slope, and size of the IAs seem to be rather important on a local scale.

Key words: Ice aprons, surface area loss, topographic factors, meteorological parameters, Mont Blanc massif.

1 Introduction

The predicted shift in climate dynamics over the next decades will undoubtedly have severe consequences on the high mountain environments, primarily on glacier extent (Rafiq and Mishra, 2016; Kraaijenbrink et al., 2017; IPCC, 2021), permafrost (Magnin et al., 2017) and ice and snow cover (Rastner et al., 2019; Guillet and Ravanel, 2020). The effects of climate change on glaciers constitute a remarkably well-discussed topic in the scientific community (Yalcin, 2019).

Meteorological parameters (mainly temperature and precipitation) are the main driving forces responsible for these changes (Scherler et al., 2011; Bolch et al., 2012; Davies et al., 2012). Shifting temperature and precipitation trends leads to the advance or retreat of glaciers both in volume and surface area (Liu et al., 2013; Yang et al., 2019). On a regional and global scale, many authors have studied the impacts of climate warming on glacier retreats and, consequently, on the hydrology of the mountain environments (*e.g.*, Baraer et al. (2012); Sorg et al. (2014); Frans et al. (2016); Coppola et al. (2018)).

However, as observed by Furbish and Andrews (1984), Oerlemans et al. (1998), Hoelzle et al. (2003) and Salerno et al. (2017), glaciers present in the same climate regime can respond to climate change in different ways. The local climate variations can partly explain these variable responses. However, many of these variations result from different morphometric (size, shape, length) and topographic (altitude, slope, aspect, curvature, terrain ruggedness) characteristics.

Several studies have been devoted to understanding the linkage between topographic factors and the response of glacier/ice bodies (*e.g.*, Davies et al., 2012; De Angelis, 2014; Salerno et al., 2017).

World Glacier Monitoring Service (WGMS) monitors glacier changes in all the major mountain regions of the world. However, most mapping and monitoring studies on a global scale focus on massive glaciers since they are generally assessable and easier to monitor compared to other ice features (Liu et al., 2013).

Studies are rare for small glaciers or ice bodies, which generally show a more pronounced response to climate change (Oerlemans and Reichert, 2000; Triglav-Čekada and Gabrovec, 2013; Fischer et al., 2015). This has led to a critical gap in our understanding of their behaviour and mass balance estimates. As part of this trend, ice aprons (IAs), sometimes also referred to as ‘rock faces partially covered with ice’ (Gruber and Haeberli, 2007; Hasler et al., 2011), have also received poor attention from the scientific community.

These small ice accumulations on steep rock slopes are commonly found in all significant glacierized basins worldwide. However, a concrete and well-summarized definition for IAs is still missing from the literature. Previously, many authors like Benn and Evans (2010), Singh et al. (2011) and Cogley et al. (2011) tried to define IAs, but the most precise definition for IAs up to now can be found in Guillet and Ravanel (2020) for the Mont-Blanc massif (MBM; European Alps). These authors defined IAs as "very small (typically smaller than 0.1 km² in extent) ice bodies of irregular outline, lying on slopes >40°, regardless of whether they are thick enough to deform under their weight". The small spatial extent of the IAs makes them very difficult to map and monitor. Also, they are typically present in extremely challenging topographies on isolated steep slopes. Cogley et al. (2011) specified that IAs are "lying above the head of a glacial bergschrund which separates the flowing glacier ice from the stagnant ice, or a rock headwall".

Because of their presence on steep slopes, IAs are essential natural elements for the practice of mountaineering, especially in famous destinations like MBM (Barker, 1982). IAs are passing points for many classic mountaineering routes (Mourey et al., 2019). Hence, the loss of IAs is a severe threat to the iconic practice of mountaineering, inscribed in 2019 by UNESCO on the Representative List of the Intangible Cultural Heritage of Humanity. IAs on steep rock walls also carry the critical role of covering steep rock slopes and preventing them from direct exposure to direct solar radiation, thus partly preventing the warming of the underlying permafrost. In addition, a recent study by Guillet et al. (2021) showed that the ice present at the base of the Triangle du Tacul IA could be older than 3 ka, making IAs a potential important glacial heritage.

Guillet and Ravanel (2020) showed that IAs in the MBM have lost mass since the Little Ice Age (LIA). Based on six different IAs, their study also showed an acceleration in the shrinkage since the 1990s. They linked the loss of IA area with meteorological parameters, mainly air temperature and precipitation. It was thus the first documented evidence that IAs have been losing ice volume due to the changing climate. However, since this study was local and based on only a few IAs, the authors could not consider other factors, such as the local topography critical for small glacier bodies (Hock, 2003; Laha et al., 2017).

Thus, to overcome these limitations, we propose a global analysis to ascertain the relationship of the area loss of IAs with the meteorological parameters, mainly air temperature and precipitation, using a more comprehensive database (*c.* 200 IAs) covering the whole MBM. The large inventory of IAs has been surveyed thanks to high-resolution aerial and satellite images from 1952, 2001, 2012 and 2019. Further, based on our inventory, we also evaluate the impacts of the topographic/geometric controls on the area changes of IAs. For this, we consider the size of IA, elevation/altitude, slope, curvature, Topographic Ruggedness Index (TRI), direct solar radiation and permafrost conditions (classified together as topographic factors) based on past studies on similar themes (*e.g.*, Oerlemans et al., 1998; Warren, 2008; DeBeer and Sharp, 2009; Jiskoot et al., 2009; Davies et al., 2012; Salerno et al., 2017).

2 Study area and the impacts of climate change in the region

The Mont-Blanc massif (Fig. 1) is located in the north-western (external) Alps between France, Switzerland, and Italy. It covers *c.* 550 km² and displays some of the highest peaks in the European Alps; a dozen peaks have elevations greater than 4000 m a.s.l. MBM thus shows a significant variation in the elevation range throughout the massif; the lowest point of the massif is at 1050 m a.s.l. (Chamonix) and the highest, the top of Mont Blanc at 4808 m a.s.l.

Because of its high elevation, the MBM is also the most glacierized massif in the French Alps (Gardent et al., 2014). There are about 100 glaciers often bordered by steep rock walls, including 12 glaciers larger than 5 km². The steep and irregular terrain facilitates the development of many unique ice bodies like cold-based hanging glaciers or IAs. Figure 2 shows two examples of the locations of the IAs on the steep N faces from the study region.

As a result of an asymmetry of the massif, 6 of the largest glaciers are located on its NW French side, where slopes are gentler than the Italian side and glaciers are well fed by the westerly winds while melting is reduced by the protection of the shaded North faces. The SE Italian side is characterized by smaller glaciers and generally steeper slopes bounded by very high sub-vertical rock walls. This asymmetry is also evidenced by the difference in the meteorological conditions observed on the two sides of the massif. For example, the Mean Annual Air Temperature (MAAT) recorded in Chamonix (at 1044 m a.s.l.) is +7.2°C while that in Courmayeur (1223 m a.s.l.) is +10.4°C (Deline et al., 2012). Comparing the annual MAAT values from 1934 to today shows that MAAT increased by > 2.1°C in Chamonix (*MétéoFrance* data). Moreover, the increase in MAAT from 1970 to 2009 was almost four times faster than from 1934 to 1970 (Mourey et al., 2019). Not only at lower elevations, but the MAAT also increased by 1.4°C at elevations exceeding 4000 m a.s.l. between 1990 and 2014 (Gilbert and Vincent, 2013). The MBM has experienced nine summers characterized by heatwaves (where maximum temperatures for at least three consecutive days exceed a heatwave temperature threshold defined for the region) since 1990 (1994, 2003, 2006, 2009, 2015, 2017, 2018, 2019 and 2020), with the one as recent as 2018 being the second (after 2003) hottest. The average annual precipitation recorded for Chamonix is 1,288 mm, and 854 mm for Courmayeur (Vincent, 2002). The precipitation rates in the MBM have remained relatively constant since the end of the LIA, but there is a noticeable decrease in the number of snowfall days relative to the total precipitation days below 2700 m a.s.l. (Serquet et al., 2011). Global warming has led to a general retreat trend of the MBM glaciers since the end of the LIA despite small re-advances culminating in 1890, the 1920s and the 1980s (Bauder et al., 2007). The recorded loss of glacier surface area was 24 % of the total area from the end of the LIA to 2008 (Gardent et al., 2014). The reported loss of ice thickness is also noteworthy. For example, the loss of ice thickness at the front of the “Mer de Glace” glacier (1650 m a.s.l.) from 1986 to 2021 is 145 m; the Argentière glacier (1900 m a.s.l.) has lost 80 m in thickness from 1994 to 2013 (Bauder et al., 2007). At 3550 m a.s.l., the surface of the Géant glacier also lowered by 20 m between 1992 and 2012 (Ravanel et al., 2013). The glacier retreat and shrinkage concur with the Equilibrium Line Altitude (ELA) that rose by 170 m between 1984 and 2010 in the western Alps (Rabatel et al., 2013). As a result of the loss of ice volume, the density of open crevasses has considerably increased, along with an increase in bare ice areas. In some instances, ice volume loss leads to instability of steep slopes, and serac falls from the front of warm and cold glaciers are more

frequent (Fischer et al., 2006). This latter process can be typical during the warmest periods of the year (Deline et al., 2012). Warming trends also intensify moraine erosion, leading to increased rockfalls and landslides (Deline et al., 2015; Ravanel et al., 2018). Degradation/warming is another critical concern for permafrost (*e.g.*, Haeberli and Gruber, 2009).

3 Data description

This section describes all the datasets obtained from diverse sources used in this study (Table. 1).

3.1 Digital Elevation Model

Since one of our study's main aims was to perform a joint analysis of the behaviour of small ice bodies and the local topography, it was paramount to have a robust high resolution and accurate Digital Elevation Model (DEM) for the study region. To avoid the uncertainties that most global DEMs are plagued with and to overcome the problem of different DEM origins on the French and Italian sides of the MBM, we built our own DEM. As part of the CNES *Kalideos Alps* project, stereoscopic sub-meter resolution optical images from the Pleiades constellation were acquired. Using the pair of stereo panchromatic images (25/08/2019), a 4 m resolution DEM was computed using the Ames Stereo Pipeline (ASP), an open-source processing chain developed by Shean et al. (2016). The parameters used for the processing were kept the same as those of Marti et al. (2016). The second part of the processing involved accurately co-registering the newly built DEM with an existing reference DEM of high precision and accuracy. For this purpose, we used the automatic DEM co-registration methodology given by Nuth and Kääb (2011). As a 'reference', we used a 2 m LiDAR DEM for the area around the Argentière glacier (8 * 2.5 km spatial extent) (Fig. 3a) built by the *Institut des Géosciences de l'Environnement* (IGE) to co-register the 'source' 4 m Pleiades DEM (Fig. 3b) generated in the previous step. A precisely co-registered, high-resolution, robust 4 m DEM was obtained at the end of the processing steps. More detailed information about the processing parameters for DEM generation and co-registration can be found in Kaushik et al., 2021. We used this DEM to compute topographic parameters like slope, aspect, curvature, elevation, TRI, mean annual rock surface temperature (MARST) and direct solar radiation.

3.2 Optical aerial and satellite images

This study relies on high-resolution aerial and satellite images (Table 1). Working with data from different sources allowed us to tap into the wealth of data for comparison. Spanning over seven decades and covering the entire MBM, ortho-images for 1952, 2001 (0.5 m resolution) and 2015 (0.2 m resolution) were downloaded from *Géoportail* IGN (French *Institut national de l'information géographique et forestière*), while the panchromatic and XS images from SPOT 6 and Pleiades at 2.2 m and 0.5 m respectively were downloaded from the *Kalideos Alps* website. Considering the small dimensions of the ice bodies, we could only work with high-resolution optical images covering the entire MBM. We were thus limited by only one set of excellent quality images for 1952 and 2001, as very high-resolution images for this study period were unavailable from any other source. Hence our mapping exercise relied only on the ortho-images for these two time periods. For 2012 and 2019, we had data from multiple sources (Pleiades, SPOT and ortho-images) to deal with the problems associated with the lack of coverage, cloud cover, illumination, shadow, and seasonal snow cover that made visual interpretation difficult. We used a combination of Pleiades and SPOT 6 XS images for mapping the IAs boundaries, with validation of results conducted with the help of the ortho-images. To avoid overestimating the extent of IAs, we utilized images acquired at the end of the summer period (late August or early September). Considering that our optical images came from many sources, it was necessary to accurately co-register all images. We used the automatic 'image to image' co-registration tool in ENVI 5.6. The process included locating and matching several feature points called tie points in a 'reference' image and a 'warped' image selected for co-registration. Here, we used the Pleiades panchromatic image of 2019 as a reference, and all the warped images were accordingly co-registered. Both coarse and fine co-registration procedures were performed, and the co-registration process was stopped when the RMSE values achieved were less than half the pixel resolution of the warped image based on the recommendations of Han and Oh (2018). A more detailed description of the co-registration process was discussed in Kaushik et al. (2021).

3.3 Meteorological data

Proxies to define accumulation and ablation phases were built to explore the correlated variations in the surface area of IAs with the changing climate. A similar study for 6 IAs was performed by Guillet and Ravanel (2020); we aim to test the validity of their results with a more extensive database (*c.*200 IAs) in the entire MBM. Since the IAs are spread across different elevation ranges, we tested the results using the SAFRAN reanalysis product (Vernay et al., 2019) that produces gridded temperature, precipitation, wind speed, and other datasets of meteorological variables at an hourly time step. This data was available as NetCDF files from 1958 for all the French massifs, at every 300 m elevation belts, at 0, 20, 40° slopes, and for all eight aspects (N, NE, E, SE, S, SW, W, NW). Our study is based on two different meteorological datasets described in the sub-sections below to compare the differences.

3.3.1 Meteorological datasets used by Guillet and Ravanel, 2020

The first part of our analysis follows a similar methodology followed by Guillet and Ravanel (2020) in their analysis. Like their study, we used homogenized weather records from the Col du Grand Saint Bernard (GSB), located close to the MBM at 2469 m a.s.l. provided by MeteoSwiss and the Aiguille du Midi (AdM) cable car station (3810 m a.s.l.). GSB represents a similar climatological regime as the MBM, and the weather records were available for an extended period starting from the 1860s. Such long-term weather records were unavailable from any weather station in the MBM. Since all IAs are located at elevations above the elevation of the GSB weather station, it was necessary to transform the weather records to an elevation closer to the average elevation range of the IAs. For this reason, it was necessary to transform the data from the GSB station using the weather records from the AdM weather station (data available since 2007). Guillet and Ravanel (2020) found a strong correlation between the monthly averaged AdM and GSB temperature records and were able to transform the GSB temperatures using a linear model:

$$T_{AdM} = \alpha T_{GSB} + \beta + r_i, \quad (1)$$

where $\alpha = 0.87$ (slope) , $\beta = -7.7^\circ \text{ C}$ (intercept) and r (residuals) with zero mean.

No transformation for the precipitation values was performed as this relation is tough to establish and not always linear (Smith, 2008). Hence, the original GSB precipitation values were used for the analysis. Using these weather records, Guillet and Ravanel (2020) found a robust correlation between ablation and accumulation proxies and the surface area change of 6 IAs. We used the same datasets to test for similar potential relationships for *c.* 200 IAs, and the results are shown in Sect. 5.3.

3.3.2 Meteorological datasets used in this study for comparison

Since the previous study involved a small number of IAs, the disparity arising from elevation differences of IAs (in turn, the temperature and precipitation coming from weather stations at a fixed elevation) could have been minimized or not well represented. We decided to use the SAFRAN reanalysis product and checked for similar potential relationships of climate variables with the surface area change of IAs. The first problem we encountered was that the SAFRAN data starts from 1958, while our first images date from 1952. Therefore, for comparison, it was essential to interpolate the missing data for the six years before 1958 (Fig. 4). Like the previous methodology, we looked for a linear relationship between the SAFRAN temperature data (at 2400 m a.s.l. elevation belt) and the GSB temperature data. We again found a strong correlation between the two datasets (Fig. 5) which helped us transform the data using:

$$T_{\text{SAFRAN2400}} = \alpha T_{\text{GSB}} + \beta + r_i, \quad (2)$$

where $\alpha = 1.01$ (slope), $\beta = -1.35^\circ \text{C}$ (intercept) and r (residuals) with zero mean.

For the SAFRAN data estimated (2400 m a.s.l.) from 1952, we extrapolated the data for all elevation bands. We used a standard gradient of $-0.53^\circ \text{C}/100 \text{ m}$ increase of elevation based on the observations of Magnin et al. (2015) for the MBM.

As previously stated, a similar relationship for precipitation was tough to establish. Hence, for the analysis, we used the SAFRAN precipitation data from 1958 and extrapolated the precipitation values from the GSB weather station to all elevation bands of SAFRAN data before 1958 (six years up to 1952). However, taking a cue from the previous study of Guillet and Ravanel (2020), we expect this impact to be insignificant when considering the results over seven decades.

4 Methods

4.1 Mapping the surface area of IAs from high-resolution satellite images

IAs boundaries were manually delineated/digitized by the first author of this paper to maintain data consistency in a GIS environment for 1952, 2001, 2012 2019. The problem of seasonal snow, which can lead to an overestimation of surface areas, was avoided using images at the end of the ablation period. The differentiation of IAs from other snow/ice bodies relies on the slope angle (we only consider ice bodies on slopes $> 40^\circ$ to be IAs) and whether they are thick enough to deform under their own weight and show movement, like in the case of hanging glaciers. The slope mask to remove areas with slopes $< 40^\circ$ was built in ArcGIS 10.6 using the Pleaides DEM. Figure 6 shows the variations in the surface areas of IAs over the study period. It also highlights the importance of high-resolution images because of the small dimensions of our study ice bodies. However, this data is not always available in the best quality for the past periods as we could only very accurately map 200 IAs (out of the total 423 IAs reported in Kaushik et al., 2021) for all the periods. These 200 IAs were selected carefully after a detailed visual inspection after considering issues related to shadow and illumination. Since a point-based correlation analysis (with meteorological and topographic parameters) requires very high accuracy and precision of mapping, any significant uncertainty would have resulted in a major bias in our correlation estimates. To avoid this, we utilize only 200 of the best mapped IAs for the correlation analysis. However, for the estimation of the total area of IAs in 1952, 2001, 2012 and 2019, as described in Sect. 5.2, we use the complete database of 423 IAs with the assumption that overall, for the entire database, the uncertainty in the mapping (\pm of the surface area) cancels out eventually and becomes insignificant.

4.2 Generation of topo-climatic parameters

The relative area loss of IAs for three time periods, *i.e.* 1952 to 2001, 2001 to 2012 and 2012 to 2019, is analyzed with all topographic factors. The area loss is expressed as a relative percentage of the area lost between the first observation and the next. Authors like Salerno et al. (2017) have also used absolute values, but for our study, this would not give a fair estimation for the analysis

as it generates a bias based on the size of IAs. The factors we considered for our analysis are elevation, slope, aspect, curvature, TRI, direct solar radiation (all estimated in ArcGIS 10.6), MARST, and size of the IAs. The topographic parameters are generated using the 4 m Pleaides DEM described in Sect. 3.1.

Direct solar radiation:

Direct solar radiation (DSR) measures the potential total insolation across a landscape or at a specific location. On a local scale, components such as topographic shading, slope, and aspect control the radiation distribution (Olson and Rupper, 2019). For estimating the DSR, the viewshed algorithm was run based on a uniform sky and a fixed atmospheric transmissivity value of 1. Sabo et al. (2016) showed the application of these algorithms in areas of rough topography. The total DSR (DSR_{tot}) for a given location is calculated as the sum of the DSR ($Dir_{\theta,\alpha}$) from all the sun sectors (calculated for every sun position at 30 minutes intervals throughout the day and month for a year):

$$DSR_{tot} = \sum DSR_{\theta,\alpha} \quad (3)$$

The direct solar radiation ($Dir_{\theta,\alpha}$) with a centroid at zenith angle (θ) and azimuth angle (α) is calculated using the following equation:

$$DSR_{\theta,\alpha} = S_{Const} * (\beta^{m(\theta)}) * SunDur_{\theta,\alpha} * SunGap_{\theta,\alpha} * \cos(AngIn_{\theta,\alpha}), \quad (4)$$

where S_{Const} is the solar constant with a value of 1367 W/m^2 , β is the transmissivity of the atmosphere (averaged over all wavelengths) for the shortest path (in the direction of the zenith), $m(\theta)$ is the relative optical path length, measured as a proportion relative to the zenith path length, $SunDur_{\theta,\alpha}$ is the time duration represented by the sky sector, $SunGap_{\theta,\alpha}$ is the gap fraction for the sun map sector and $AngIn_{\theta,\alpha}$ is the angle of incidence between the centroid of the sky sector and the axis normal to the surface.

The final map of DSR is the sum of values calculated at an hourly time step for every pixel, as per the resolution of the DEM used. The values of solar radiation are given in W/m^2 . Higher values for solar radiation indicate higher insolation, while lower values suggest low insolation. We prefer

DSR over the aspect for our analysis to avoid bias due to local shading on sun-exposed faces, considering the slope angle associated with the aspect.

Elevation:

Elevation strongly influences the meteorological conditions within the same region, significantly altering the precipitation, temperature, and wind regime even at a local scale. Generally, higher elevations receive more precipitation and experience lower temperatures and higher wind speeds. Hence regions at higher elevations, especially above the ELA, should favour more accumulation than ablation. However, wind-driven snow at higher elevations does not readily accumulate on steep slopes. Some IAs may take advantage of the leeward conditions at lower elevations and sustain for more extended periods. Similar results for large glaciers have previously been reported by Bhambri et al. (2011) or Pandey and Venkataraman (2013).

Mean slope:

Slope angle strongly influences ice velocities of glaciers, mass flux, and the hydrology of the mountain environments. Its influence on avalanche transport of snow over the glacier surface has been discussed previously (*e.g.*, Oerlemans, 1989; Hoelzle et al., 2003; DeBeer and Sharp, 2009). Numerous studies have also reported that slope is the single most crucial terrain parameter that controls glacier responses to climate change (Furbish and Andrews, 1984; Oerlemans et al., 1998; Jiskoot et al., 2009; Scherler et al., 2011). In mountainous regions, the terrain slope strongly influences snow accumulation. On steep slopes, accumulation in the temperature range of -5 - 0°C can accumulate on steep slopes. Slope likewise plays a key role when calculating other terrain parameters and indices.

Mean annual rock surface temperature:

MARST estimates the average annual temperature of the rock surface governed mainly by the incoming shortwave solar radiation (PISR) and the mean annual air temperature (MAAT). The method for estimating MARST is described by Boeckli et al. (2012) and Magnin et al. (2019). The estimation is based on a multiple linear regression model with the form:

$$Y = \alpha + \sum_{i=1}^k \theta_i X^i + \varepsilon,$$

where Y is the value for MARST, α is the intercept term, $\theta_i X^i$ represents the model's k variables (PISR and MAAT) and their respective coefficients, and ε residual error term distributed equally with the mean equal to 0 and the variance $\sigma^2 > 0$. For predicting the values of MARST in steep slopes, we use the equation:

$$\text{MARST}_{(\text{pred})} = \alpha + \text{PISR} * b + \text{MAAT} * c, \quad (6)$$

where α is the $\text{MARST}_{\text{pred}}$ value when PISR and MAAT are equal to 0, and b and c are the respective coefficients of PISR and MAAT at measured RST positions. These coefficients were calibrated by Boeckli et al. (2012) (rock model 2) for the entire European Alps using a set of 53 MARST measurement points. The MAAT of the 1961-1990 period was used to calculate MARST, representing a steady state.

The values for MARST are calculated in °C and, for our study region, range from -12 to 10°C. MARST is also an important criterion to check for the very likely presence of permafrost below the IAs, which likely allows the formation and existence of IAs.

Topographic Ruggedness Index:

The topographic Ruggedness Index (TRI) measures the ruggedness of the landscape. TRI was calculated based on the methodology proposed by Sappington et al. (2007). It is calculated as a 3-dimensional dispersion of vectors (x , y , z components) normal to the grid cells considering the slope and aspect of the cell. The magnitude of the resultant vector in a standardized form (vector strength divided by the number of cells in the neighbourhood) measures the ruggedness of the landscape. Higher values of TRI thus suggest a more rugged and sporadic terrain, which could block the downward movement of the snow and subsequently lead to the formation of a weak layer, destabilizing the snowpack and leading to small avalanches resulting in mass wasting (Schweizer, 2003). Since IA surfaces are smooth, the TRI values calculated at the surface of the IA are always low. Hence, we consider the TRI values by taking a buffer of 20 m around the IA

boundary delineated for the first observation (1952). The mean TRI value from this buffer is considered for our analysis.

Curvature:

Curvature, estimated as a second derivative of the surface, defines the shape of the slope. Curvature is considered an essential factor because it can define snow accumulation or ablation rates for a surface. Generally, two types of curvature profiles are known, plan and profile. For our analysis, we only used the profile curvature as it defines the shape of the slope in the steepest direction. From a theoretical point of view, erosion processes prevail in convex (negative values) profile curvature locations, while deposition is predominant in concave (positive values) profile curvature locations. The curvature values define how strongly the slope is convex (lower negative values) or concave (higher positive values). That is why curvatures can be considered essential in the accumulation and ablation rates of a glacier or ice body. Like TRI, the IAs tend to show flat curvature profiles if we consider their surface. Hence, we estimate the curvature values around the same buffer as the TRI and use this for further analysis.

4.3 Proxies for ablation and accumulation

To eventually correlate changes in surface area of IAs with the changing climate, we use the temperature and precipitation data from the transformed GSB weather records and SAFRAN reanalysis product (see Sect. 3.3) to build proxies for accumulation and ablation. The proxy for ablation was built by estimating the annual sum of positive degree-days (PDD) computed from the normal probability distribution centered around the mean monthly temperature. Estimation of the PDD is based on the empirical relation, which states that the melting rate is proportional to the surface-air temperature excess above 0°C. Several methods for estimating PDD have been proposed by Braithwaite and Olesen (1989), Braithwaite (1995), and Hock (2003). However, the method proposed by Calov and Greve (2005) also accounts for stochastic variations in temperature during the computation of PDD. The formula for the estimation of the PDD using this method is given by:

$$PDD = \int_0^A dt \left[\frac{T_{ac}^2}{\sqrt{2\pi}} \exp\left(-\frac{T_{ac}}{2\sigma^2}\right) + \frac{T_{ac}}{2} \operatorname{erfc}\left(-\frac{T_{ac}}{\sqrt{2}\sigma}\right) \right] \quad (7)$$

T_{ac} is the annual temperature cycle (monthly mean temperatures estimated in °C for the entire year), σ is the standard deviation of the temperature from the annual cycle, $A = 1$ year, and erfc is the conventional error function built-in in all programming languages.

After computing the PDD, we calculate the cumulative PDD (CPDD) by taking the sum of all the annual PDD values for each observation period (*i.e.* 1952-2001, 2001-2012 and 2012-2019). This value of CPDD is then used as a proxy for ablation (Braithwaite and Olesen, 1989; Vincent and Vallon, 1997).

The calculation of the proxy for accumulation is more tricky because we only consider the yearly sum of precipitation occurring at a temperature between -5 and 0° C, as only snowfall within this temperature range is believed to accumulate/adhere to steep slopes (Kuroiwa et al., 1967; Guillet and Ravanel, 2020; Eidevåg et al., 2022). The temperature-dependent indicator function can be written in the following form:

$$\chi_i(T, (t)) = \begin{cases} 1 & \text{if } -5^\circ\text{C} \leq T(t) \leq 0^\circ\text{C} \\ 0 & \text{otherwise} \end{cases} \quad (8)$$

4.4 Surface area model

Using the proxy for ablation and accumulation, Guillet and Ravanel (2020) proposed a surface area model to estimate the differences in the surface areas of IAs between different time steps due to the time-integrated changes in meteorological parameters. The main goal is to look for a potential linear relationship between climate variables and the changes in surface areas of IAs, using a multivariate regression model. The equation for the model can be written as:

$$S_m(t) = S(t_0) - \int_{t_0}^t (\alpha_1 CPDD(t) - \chi_i(T(t))\alpha_2 A(t))dt + \beta + \varepsilon(t) \quad (9)$$

where $S_m(t)$ corresponds to the modelled surface area at time t ; similarly, $CPDD(t)$ and $A(t)$ represent the proxies for ablation and accumulation; $S(t = 0)$ is the first available measurement; α_1 and α_2 are the coefficients of linear regression, β is the intercept, and ϵ the residual. $\chi(T, t)$ accounts for precipitation occurring in the $[-5^\circ\text{C}, 0^\circ\text{C}]$ temperature range and is given by the temperature-dependent indicator function given in equation (8). The area of IAs at each time step was calculated using the surface area model (with the temperature and precipitation proxies), and we hereafter refer to this area as modelled area. The measured area is the surface area we delineated using high-resolution optical images.

4.5 Uncertainty estimations

Since this study uses data from different sources and periods, uncertainties of different origins might have been introduced to delineate the IA boundaries. A good estimation of these uncertainties is thus crucial to have a fair estimation of the significance of the results (Racoviteanu et al., 2008; Shukla and Qadir, 2016; Garg et al., 2017). Some sources of uncertainty in this study could arise from (1) errors inherent to the aerial images and satellite-derived datasets, (2) errors resulting from inaccurate co-registration of data from various sources, (3) errors produced while generating the high-resolution DEM from stereo images, and (4) conceptual errors linked with defining the boundaries of IAs in all images. Quantifying the errors inherent in processing all datasets used is challenging, and this is out of the scope of this paper. A detailed accuracy assessment of the DEM generation and co-registration process is provided in Sect. 5.1 and 3.1, respectively. Quantifying errors resulting from the manual delineation of IA boundary is also challenging, but we have previous guidelines from Paul et al. (2017) for the quality and consistency assessment of manual delineations.

One way to assess the area uncertainty is to perform multiple digitizations of the same surface and calculate the mean area deviation (MAD), taking the first digitization as a reference (Meier et al., 2018). Considering this, the first author performed three digitizations for 50 IAs on images from 1952, 2001, 2012 and 2019, considering different challenges associated with aerial and satellite images like shadow and illumination. MAD provides a percentage estimate of how the final area calculated varies across multiple digitizations for each polygon. MAD values are affected by the size of the polygon manually digitized. Previously, authors like Paul et al. (2013), Fischer et al.

(2014) and Pfeffer et al. (2014) have reported an increase in the uncertainty of manual digitizations with a decrease in the size of the polygons. With this in mind, we also digitized IAs of different sizes ranging from 0.001 km² to 0.01 km².

5 Results

5.1 Accuracy of the DEM

Figure 7a shows the stable surfaces (after eliminating glacier boundaries, trees, and forests) we used for our co-registration process, and Figure 7b displays the difference in elevation between the reference DEM and the source DEM before co-registration. Figure 7c presents the results after the co-registration process considering all the surfaces (stable and non-stable), and Figure 7d shows the difference considering only the stable areas after masking out non-stable areas using the glacier boundaries provided by the RGI. The source DEM was translated using the corresponding shift values $x = -5.03$ m, $y = 6.00$ m, and $z = 3.22$ m

The distribution of errors can be visualized by a histogram of the sampled errors, where the number of errors (frequency) within certain predefined intervals is plotted (Höhle and Höhle, 2009). Figure 8 shows the histogram of the errors Δh (elevation difference between the reference and source DEM) in meters for the stable areas. The accuracy estimates before and after the co-registration are shown by the normalized median absolute deviation (nmad) and the median value calculated together. As can be seen, the nmad and median values before the co-registration process for stable areas were 5.16 and -5.06, respectively. After the co-registration process, the value dropped to 1.98 for the nmad and -0.14 for the median value. This suggests a good correlation between the high-resolution LiDAR DEM used as a reference and the Pleiades DEM we built.

5.2 Total area loss of ice aprons in the Mont-Blanc massif over seven decades

The total area of IAs mapped in 1952 was 7.932 km². It dropped to 5.915 km² in 2001. The surface area dropped to 4.919 km² in 2012 and then to 4.21 km² in 2019 (Fig. 9). This implies that from 1952 to 2019, IAs have lost ~47 % of their original area in 67 years. It corresponds to an average surface area loss of 0.78 km² per decade. However, the percentage area loss from 1952 to 2001 was ~25 % compared to ~29 % relative area loss from 2001 to 2019. This is an alarming rate: IAs have lost more relative area during the 18 recent years (with an average area loss of 1.15 %/ year) compared to the 50 years before 2001 (0.5 %/ year average area loss).

Figure 10 shows the MAD values for 50 IAs in 1952, 2001, 2012 and 2019. We did not observe an increase in MAD values with decreasing size of the IAs, mainly because the number of samples we used is comparatively less than that in the previous studies. Overall, the mean MAD observed for all years was ± 6.4 %. The MAD for the IAs digitized on the orthophotos from 1952 was ± 6.68 %, while for 2001, it was ± 7.2 %. The MAD for 2012 and 2019 was ± 6.32 % and ± 5.50 %, respectively.

5.3 Influence of changing climate on the area loss

Figure 11 shows the trend of PDD increase over the years in the MBM. All elevations, except 4800 m a.s.l., show an increasing trend of PDD values from 1952 to 2019. Specifically, for the year 1952, since we have only one year for the longer-term analysis, it is interesting to look in detail at the climatic conditions prevailing in the region around this period. Looking at the GSB records, the average temperature in the region during the past ten years before 1952 was -0.987 °C, with average summer temperatures (July, August and September) being 6.783 °C. 1947 was particularly hot, with the annual average temperature recorded at -0.275 °C and average summer temperatures at 8.266 °C. The next thirty years after 1952 were more favourable, with average annual temperatures recorded at -1.523 °C and average summer temperatures being 5.256 °C (GSB data provided as supplementary material 1). Since 1952 was coming at the back of considerably warmer years, a significant reduction in their surface area can be expected during this period. Looking at the weather records, the conditions after 1952 for the next thirty years were more favourable.

Similarly, Figure 12 shows the variations in the accumulation rates (average annual accumulation per period) for all elevation bands. The results show only that part of the snowfall which is expected to accumulate on the steep slopes. Except for the highest elevation band, i.e. 4800 m a.s.l. accumulation rates at all elevation bands show a general decreasing trend. For example, at the 3900 m a.s.l. elevation band, accumulation rates fell from 32mm/year from 1952 -2001 to 28 mm/year from 2001 to 2012, and further to 18 mm/year between 2012 – 2019. This shows that temperatures in the MBM are increasing, while on the other hand, accumulation on steep slopes is decreasing over time. Figure 13 shows the annual variation of the accumulation on steep slopes at different elevations. The first observation from this trend shows that very little precipitation accumulates on steep slopes in the winter months, while accumulation occurs almost entirely in the summer months. Further, the accumulation is more significant at higher elevations (4200 – 4500 m a.s.l.) in the summer months than at lower elevations. At lower elevations, accumulation is predominantly observed in pre-summer (May) and post-summer (October) months.

Figure 14a presents the correlation between the ratio of the mean measured surface area at time t , $S(t)$, to the initial area, $S(t_0)$, with the ratio of the mean modelled surface area using the GSB transformed data to the initial area for 2001 and 1952. We consider the ratio of $S(t)/S(t_0)$ as an indicator to estimate the area loss between the two time periods. A high ratio value (*i.e.* value close to 1) in the present context indicates that the relative surface area loss of IAs between the two periods is comparatively less than that of IAs whose ratio is closer to 0. A value larger than 1 indicates an increase in the surface area over time.

From the results, we do not see a strong correlation ($r = 0.73$) between the modelled area (from GSB transformed climate data) and the measured area for the 200 IAs spread across the MBM (Fig. 14 a). However, the correlation improves significantly ($r = 0.86$) when we use the SAFRAN data based on different elevations and remodel the surface area for each IA (Fig. 14 b). This can be seen from the values of R^2 , Pearson's r , RMSE and the p-value estimates from the T-test achieved from both datasets (Table 2). The best-fitting line presents a slope of 1.0 and an intercept of 0.0.

Both figures show that IAs at lower elevations (blue to green colour and small tick size) generally show lower ratios values than IAs at higher elevations (yellowish colours and bigger tick size). This implies that the elevation of the IAs potentially plays a crucial role in their response to the changing climate. Overall, the surface area of IAs decreased throughout the massif from 1952 to

2001 except for 4 IAs, which showed an increase in surface area. These 4 IAs are: 2 IAs on the N and NW face of Rochers Rouges Inferieurs (~4350 m a.s.l. and 4050 m a.s.l.) near the Grand Plateau, 1 IA on the NE face of Col de la Brenva (~4160 m a.s.l.) and 1 IA on the S face of Col du Bionnassay (~4050 m a.s.l.). As observed, all these IAs are located at elevations higher than 4000 m a.s.l. As an exception, it can be expected that a few IAs could show an increase in the surface area. However, this increase is not dramatic (~10 % increase). The results, however, reaffirm the proficiency of the proposed surface area model in predicting new IA states from the accumulation and ablation proxies. Similar results were observed for the other two time periods, *i.e.* 2001-2012 and 2012-2019, as seen in Table 2.

5.4 Influence of the local topography and other factors on the area loss of IAs

Each parameter, as described in Sect. 4.2 was individually regressed with the relative area loss of IAs for the three periods, and their influence was assessed by the coefficient of determination (R^2) and Pearson's r-value.

A joint analysis of the surface area lost by the IAs and the direct solar radiation reveals a strong correlation between the values of DSR and the relative surface area loss of IAs for all the three-time periods (1952-2001, 2001-2012 and 2012-2019) (Fig. 15a; Table 3). However, this is the first evidence of the potential negative impact of solar radiation on small ice bodies like IAs. Previous analysis of Guillet and Ravel, 2020 with the climate variables indicated a potential relationship between the elevation and the surface area loss of IAs. This is somewhat statistically significant from the regression analysis, as we found a negative correlation between the surface area loss and the mean elevation of the IAs (Fig. 15b; Table 3). A further comparison of the IAs (200 IAs) distribution with elevation and aspect shows that most IAs (~ 77 % of the total number) exist at elevations above 3200 m a.s.l. Further, most IAs (~ 56.5 %) exist in the northern aspects (N, NW, NE), while the E and W aspects are the least favoured (supplementary material 2). In addition, we found a moderate positive correlation between the average MARST values and the surface area loss of IAs. The correlation observed was not very significant compared to the previous two factors. It indicates that the effect of rock surface temperatures on the area loss of IAs is not strong on a regional scale. (Fig. 15c; Table 3). However, this relationship needs to be examined in a more

site-specific and localized area to understand better its impact on the surface area loss of IAs. We also observed that the correlation was higher for a more extensive observation period (1952-2001) than for shorter periods. This could suggest that the influence of rock surface temperatures potentially becomes more prominent with a more extensive observation period.

A similar analysis of IA area loss with the TRI showed a weak positive correlation (Fig. 15d; Table 3). An increase in TRI values (*i.e.* increase in terrain ruggedness) may result in more ice area loss on a site-specific scale, but this relationship is hard to observe globally. Like the results from the analysis with MARST, the strongest correlation was again observed for the largest study period. Further, like the TRI, we also found a weak correlation between the terrain slope and curvature with the surface area loss of IAs. We must note that our criteria for selecting IAs already limit us to areas with slope angles steeper than 40° (Fig. 15e; Table 3). Hence it was difficult to observe any significant impact of terrain slope on the rate of area loss of IAs. Similarly, terrain curvature seems to have the most negligible impact (Fig. 15f; Table 3). As cited in Sect. 4.2. previous studies may have shown that terrain curvatures could play an essential role in the erosion and accumulation dynamics on steep slopes, but this is not the case for IAs in the MBM. We performed the last comparison between the relative surface area loss of IAs with their initial area. Our results were similar to the one Lopez et al. (2010) reported, as we did not find any correlation between the two quantities (Fig. 15g; Table 3).

6. Discussion:

6.1 Area loss of ice aprons and the role of the changing climate

As observed from the results in Sect. 5.2, IAs have been losing surface area at an alarming rate. This rate of surface area loss is disconcerting because, compared to the glaciers in the MBM, the IAs are losing their area at a higher rate (~24 % for glaciers from the end of LIA till 2008, according to Gardent et al., 2014, while IAs have lost ~47% surface area in the last 70 years). The small size of IAs makes them more vulnerable to global warming than large glaciers. An increase in average annual temperatures and a decrease in precipitation rates puts the existing IAs at risk of losing their mass entirely before the end of this century. In addition, considering that the effects of local

topography are also more pronounced in the case of IAs than for large glaciers, continuous monitoring of these critical ice bodies has become imperative. Results discussed in Sect. 5.3 indicated the strong influence of temperature and precipitation on the surface area changes of IAs. The results raise further questions regarding the sensitivity of the IAs to extreme weather events, like the heatwaves experienced in the study region. Unfortunately, our sampling rate does not allow us to quantify the effects of individual extreme weather events. Nevertheless, there is a strong argument in favour that these events, especially in the past two decades, cause the IAs to lose mass more rapidly than in the previous decades. Further, the heatwaves occurring during winter and midsummer, when the IA surfaces are free of snow, will have the worst adverse effect. As suggested by Meehl and Tebaldi, (2004), with an increase in the intensity and frequency of extreme events in the coming decades, understanding the effects of climate variables on the sensitivity of IAs is even more critical.

Further, several authors have previously also accounted for the variations in solar radiation in mass-balance modelling studies (Huss et al., 2009; Thibert et al., 2018). Our results showed a strong correlation of DSR with area change, making this argument stronger. However, since the focus was to show the impact of climate variables separately, we preferred a temperature-index model as the first approach. However, we expect solar radiation to play a significant role in the sensitivity of ice aprons, and future studies on ice apron evolutions in the 21st century should address this question.

6.2. Area loss of ice aprons and the role of topographic parameters

Since ice/glacier bodies within the same climate regime can also respond to climate change differently, the last part of the analysis (Sect. 5.4) was dedicated to understanding the linkages of local topographic factors to the surface area loss of IAs. As reported previously by Salerno et al., 2017 some local topographic factors influence the response of IAs to climate change more significantly than the others. A first analysis showed that IAs that receive more solar radiation from the sun throughout the year lose their surface area faster than those that receive less DSR. Similar results for other regions in mountain environments have also been reported previously by Oerlemans and Klok (2002); Mölg (2004); Johnson and Rupper (2020). Incoming solar radiation

is an essential component of all surface energy and mass balance models. But the significance of DSR on the surface area loss of small ice bodies like IAs is reported for the first time in our study. Further, the correlation between elevation and surface area loss of IAs was the second most significant of all topographic factors. IAs located at lower elevations are potentially subject to more intense degradation and lose their surface area faster than those at higher elevations. On a more local scale, other topographic factors could also play a critical role in the surface area variations of IAs. However, elevation seems to be a dominant causative factor on a regional scale. Elevation strongly influences meteorological conditions (temperature, precipitation, and wind speeds) and permafrost; this likely strongly influences the durability of IAs in the context of changing climate. Hantel et al. (2012) suggested that the median summer snowline for the Alps to be at 3083 ± 121 m a.s.l. (1961 – 2010), while Rabatel et al. (2013) documented the regional ELA at 3035 ± 120 m a.s.l. (1984 – 2010). Rabatel et al., 2013 further described the rising of the ELA to 3250 ± 135 m a.s.l. during the 2003 heatwave. Subsequent heatwaves of 2006, 2015 and 2019 would have likely resulted in similar scenarios (Hoy et al., 2017). Since ~77 % of the total IAs reported in this study exist at elevations above 3200 m a.s.l., the rising of the ELA in future climate scenarios risks more IAs towards faster degradation and disappearance. An example of this is the case of the IA on the north face of Aiguille des Grands Charmoz (3445 m a.s.l.), which completely disappeared during the 2017 summer heatwave (Guillet and Ravanel, 2020).

In addition, on a local scale, some correlation between the rock surface temperatures and the area loss of IAs was observed from the analysis. Guillet et al. (2021) suggested that IAs are cold ice bodies that exist predominantly on permafrost-affected rock walls. They further reported temperatures $<0^{\circ}\text{C}$ at the base of the ice core taken from the IA on the north face of Triangle du Tacul (3970 m a.s.l.). Heating from rock surfaces is predominantly the cause of permafrost degradation, which further affects mountain slope stability leading to an increased rock mass wasting (Magnin et al., 2017). Cold surfaces demonstrate more ice cohesion with the underlying surfaces, while a rise in surface temperatures decreases basal cohesion, increasing the sliding process and leading to more ice flow (Deline et al., 2015). Thus, it is likely that underlying permafrost conditions aid the sustainability of IAs in the long term, and an increase in rock surface temperatures around IAs could result in IAs losing mass more rapidly.

Kaushik et al. (2021) further showed that most IAs exist in extremely rugged terrains: 51 % of the total IAs mapped exist in the TRI's high and very high ruggedness class, while only 8 % exist in

the low ruggedness. Thus, comparing the terrain ruggedness to the area loss of IAs makes sense since the topography around the snow/ice bodies can critically influence their stability (Deline et al., 2015). Increasing terrain ruggedness is associated with slope instability and further ice volume loss. However, for our study, this relation was not very pronounced, showing that the topography's ruggedness does not substantially affect the area loss of IAs.

Previous analysis by Kaushik et al., 2021 also showed that most IAs in the MBM (83 %) lie at mean slopes between 40° and 65° . Increasing slope steepness limits accumulation, while avalanches further scour away snow from the surface of the IA, thus exposing the ice directly to the sun and wind (Vionnet et al., 2012). However, the differences in slope angles of the IAs were not a dominant factor affecting the rates of area loss. A plausible explanation for this could be that since we limit the slope criteria to $>40^{\circ}$ and most IAs lie in the range of 40 to 65° slope, the effect of terrain slope is not as well pronounced as it would be between low ($< 15^{\circ}$) and extreme slopes ($>65^{\circ}$). Similar results were observed by Li et al. (2011), as they observed very slight variations in area loss for small glaciers with differences in slope. They suggested other local topographic factors could mitigate the effects of slope in case of small ice/snow bodies.

Similarly, terrain curvature also has a negligible effect on the surface area loss of IAs. As suggested by Alkhasawneh et al., 2013; Yanuarsyah and Khairiah, 2017, convex profile curvature favours the erosion processes, while in locations with concave curvature, the deposition process can be predominant. Over time, the terrain curvature can be a dominant factor in the dynamics of glacier/ice bodies, but this relation was not established for our study.

At last, a comparison of the rate of surface area loss of IAs with the original size of the IAs was performed, and we observed no correlation between the two factors. Although previous studies by Paul et al. (2004), Jiskoot et al. (2009), and Garg et al. (2017) have shown the correlation between the size of the ice/glacier bodies with the area loss, this is not evident in our case. Unlike previous studies, which considered different glaciers ranging in size from less than a km^2 to several hundred km^2 , IAs are small ice bodies (0.0005 km^2 to 0.1 km^2). Hence, it is plausible that the effect of IA size on area loss rate is not pronounced in our case. Similar results were shown by Lopez et al. (2010), who analyzed 72 glaciers in South America, and reported no correlation between the glacier length and the area loss of glaciers.

Another critical factor to consider, along with the impact of topography, is the role of avalanches in the erosion and deposition processes on the IA surface. Analysis of the ice core from the N- face

of Triangle du Tacul showed that IAs are almost immobile cold ice bodies (Guillet et al., 2021). Hence IAs do not directly participate in feeding the larger glacier systems below them. However, the avalanches triggered above can bring fresh snow/debris and lead to erosion or deposition on the IA surface. We expect this factor to also play a role in the area change dynamics of the IA, which we have not considered a part of this study. Although this impact on the scale of an IA is tough to determine, future studies should focus on ascertaining this impact at least on a local site-specific scale.

7. Conclusions

This study makes the first attempt to understand the dynamics of IAs concerning the changing climate and topographic factors at a regional scale. IAs are very small ice features but highly critical components of the mountain cryosphere. Because of the difficulties associated with their monitoring and relative unimportance to mountain hydrology, no studies solely based on their evolution on a regional scale have been performed before. This paper presented an analysis of 200 IAs spread throughout the MBM and existing in different topographic settings to understand their dynamics in the context of climate warming. For this purpose, we accurately mapped the IAs on very high-resolution aerial and satellite images available for 1952, 2001, 2012 and 2019. Using our extensive database of IAs, we compared the total area variation of IAs for three periods. Further, we also attempted to establish a relationship between the surface area lost by IAs with meteorological parameters (*i.e.* temperature and precipitation) and their associated topographic parameters.

Some important outcomes from the study are:

- Over the study period 1952-2019, IAs have lost their surface area at a very alarming rate. The total area of IAs in MBM was 7.93 km² in 1952, which dropped to 5.91 km² in 2001, to 4.91 km² in 2012, and at last to 4.21 km² in 2019 (~ 47% drop in total surface area in less than three-quarters of a century).
- The observed rate of relative area loss in the last 18 years (~29 %) is more than the overall area loss during the 48 previous years (1952-2001; ~ 26 %).

- Results from the analysis of IAs surface area loss and meteorological parameters conclusively proved the strong impact of meteorological parameters (i.e. temperature and precipitation) on the behaviour of small ice bodies like IAs.
- Further analysis of IAs surface area loss with different topographic parameters showed a strong correlation of IAs surface area loss with the DSR and elevation. Other factors like MARST, TRI, and mean terrain slope could also play an important role locally, but their effect is not significant regionally. Other factors like terrain curvature and the size of the IAs were not found to significantly impact the IA's surface area loss.

Looking at the melting rate of IAs and the future predictions of global climate change, it is evident that these small and critical ice bodies are most vulnerable to adverse impacts. It is hard to imagine any of the IAs surviving the next few decades with increasing temperatures at the present and future melting rates. The loss of IAs will thus be the loss of crucial glacial heritages and playgrounds for the iconic practice of mountaineering. Hopefully, this study forms a basis to encourage further studies on IAs.

Author contributions: SK designed the study and drafted the paper, which all co-authors revised. LR and FM helped in data interpretation and analysis. YY and ET proofread the manuscript and provided valuable inputs for improving the overall quality of the paper. DC processed and provided the DEM used for the study.

Data availability: The ice apron inventory will be made available on demand.

Competing Interests: The authors declare that they have no conflict of interest.

Acknowledgements:

This research is part of the USMB *Couv2Glas* and *GPClim* projects. Pleiades data were acquired within the CNES *Kalideos-Alpes* project and successfully processed under the program "*Emerging risks related to the 'dark side' Alpine cryosphere*". We also thank C. Vincent of the *Institut des*

794 *Géosciences de l'Environnement* (IGE) for providing the LiDAR DEM of the Argentière glacier
795 area.

796

797

798 **References:**

799 Alkhasawneh, M. Sh., Ngah, U. K., Tay, L. T., Mat Isa, N. A., and Al-batah, M. S.: Determination of
800 Important Topographic Factors for Landslide Mapping Analysis Using MLP Network, *The Scientific World*
801 *Journal*, 2013, 1–12, <https://doi.org/10.1155/2013/415023>, 2013.

802 Allen, T. R.: Topographic context of glaciers and perennial snowfields, Glacier National Park, Montana,
803 *Geomorphology*, 21, 207–216, [https://doi.org/10.1016/S0169-555X\(97\)00059-7](https://doi.org/10.1016/S0169-555X(97)00059-7), 1998.

804 Barker, M. L.: Traditional Landscape and Mass Tourism in the Alps, *Geographical Review*, 72, 395,
805 <https://doi.org/10.2307/214593>, 1982.

806 Bauder, A., Funk, M., and Huss, M.: Ice-volume changes of selected glaciers in the Swiss Alps since the
807 end of the 19th century, *Ann. Glaciol.*, 46, 145–149, <https://doi.org/10.3189/172756407782871701>,
808 2007.

809 Benn, D. I. and Evans, D. J. A.: *Glaciers & glaciation*, 2nd ed., Hodder education, London, 2010.

810 Bhambri, R., Bolch, T., Chaujar, R. K., and Kulshreshtha, S. C.: Glacier changes in the Garhwal Himalaya,
811 India, from 1968 to 2006 based on remote sensing, *J. Glaciol.*, 57, 543–556,
812 <https://doi.org/10.3189/002214311796905604>, 2011.

813 Boeckli, L., Brenning, A., Gruber, S., and Noetzli, J.: Permafrost distribution in the European Alps:
814 calculation and evaluation of an index map and summary statistics, *The Cryosphere*, 6, 807–820,
815 <https://doi.org/10.5194/tc-6-807-2012>, 2012.

816 Bolch, T., Kulkarni, A., Kaab, A., Huggel, C., Paul, F., Cogley, J. G., Frey, H., Kargel, J. S., Fujita, K., Scheel,
817 M., Bajracharya, S., and Stoffel, M.: The State and Fate of Himalayan Glaciers, *Science*, 336, 310–314,
818 <https://doi.org/10.1126/science.1215828>, 2012.

819 Braithwaite, R. J.: Positive degree-day factors for ablation on the Greenland ice sheet studied by energy-
820 balance modelling, *J. Glaciol.*, 41, 153–160, <https://doi.org/10.3189/S0022143000017846>, 1995.

821 Braithwaite, R. J. and Olesen, O. B.: Calculation of Glacier Ablation from Air Temperature, West
822 Greenland, in: *Glacier Fluctuations and Climatic Change*, vol. 6, edited by: Oerlemans, J., Springer
823 Netherlands, Dordrecht, 219–233, https://doi.org/10.1007/978-94-015-7823-3_15, 1989.

824 Calov, R. and Greve, R.: A semi-analytical solution for the positive degree-day model with stochastic
825 temperature variations, *J. Glaciol.*, 51, 173–175, <https://doi.org/10.3189/172756505781829601>, 2005.

826 Cogley, J. G., Hock, R., Rasmussen, L. A., Arendt, A. A., Bauder, A., Braithwaite, R. J., Jansson, P., Kaser,
827 G., Möller, M., Nicholson, L., and Zemp, M.: Glossary of glacier mass balance and related terms,
828 <https://doi.org/10.5167/UZH-53475>, 2011.

829 Davies, B. J., Carrivick, J. L., Glasser, N. F., Hambrey, M. J., and Smellie, J. L.: Variable glacier response to
830 atmospheric warming, northern Antarctic Peninsula, 1988–2009, *The Cryosphere*, 6, 1031–1048,
831 <https://doi.org/10.5194/tc-6-1031-2012>, 2012.

832 De Angelis, H.: Hypsometry and sensitivity of the mass balance to changes in equilibrium-line altitude:
833 the case of the Southern Patagonia Icefield, *J. Glaciol.*, 60, 14–28,
834 <https://doi.org/10.3189/2014JoG13J127>, 2014.

835 DeBeer, C. M. and Sharp, M. J.: Topographic influences on recent changes of very small glaciers in the
836 Monashee Mountains, British Columbia, Canada, *J. Glaciol.*, 55, 691–700,
837 <https://doi.org/10.3189/002214309789470851>, 2009.

838 Deline, P., Gardent, M., Magnin, F., and Ravel, L.: The morphodynamics of the mont blanc massif in a
839 changing cryosphere: a comprehensive review, *Geografiska Annaler: Series A, Physical Geography*, 94,
840 265–283, <https://doi.org/10.1111/j.1468-0459.2012.00467.x>, 2012.

841 Deline, P., Gruber, S., Delaloye, R., Fischer, L., Geertsema, M., Giardino, M., Hasler, A., Kirkbride, M.,
842 Krautblatter, M., Magnin, F., McColl, S., Ravel, L., and Schoeneich, P.: Ice Loss and Slope Stability in
843 High-Mountain Regions, in: *Snow and Ice-Related Hazards, Risks and Disasters*, Elsevier, 521–561,
844 <https://doi.org/10.1016/B978-0-12-394849-6.00015-9>, 2015.

845 Dodson, R. and Marks, D.: Daily air temperature interpolated at high spatial resolution over a large
846 mountainous region, *Clim. Res.*, 8, 1–20, <https://doi.org/10.3354/cr008001>, 1997.

847 Eidevåg, T., Thomson, E. S., Kallin, D., Casselgren, J., and Rasmuson, A.: Angle of repose of snow: An
848 experimental study on cohesive properties, *Cold Regions Science and Technology*, 194, 103470,
849 <https://doi.org/10.1016/j.coldregions.2021.103470>, 2022.

850 Fischer, L., Käab, A., Huggel, C., and Noetzli, J.: Geology, glacier retreat and permafrost degradation as
851 controlling factors of slope instabilities in a high-mountain rock wall: the Monte Rosa east face, *Nat.*
852 *Hazards Earth Syst. Sci.*, 6, 761–772, <https://doi.org/10.5194/nhess-6-761-2006>, 2006.

853 Fischer, M., Huss, M., and Hoelzle, M.: Surface elevation and mass changes of all Swiss glaciers 1980–
854 2010, *The Cryosphere*, 9, 525–540, <https://doi.org/10.5194/tc-9-525-2015>, 2015.

855 Frans, C., Istanbuluoglu, E., Lettenmaier, D. P., Clarke, G., Bohn, T. J., and Stumbaugh, M.: Implications
856 of decadal to century scale glacio-hydrological change for water resources of the Hood River basin, OR,
857 USA: Hydrological Change in the Hood River Basin, *Hydrol. Process.*, <https://doi.org/10.1002/hyp.10872>,
858 2016.

859 Furbish, D. J. and Andrews, J. T.: The Use of Hypsometry to Indicate Long-Term Stability and Response of
860 Valley Glaciers to Changes in Mass Transfer, *J. Glaciol.*, 30, 199–211,
861 <https://doi.org/10.1017/S0022143000005931>, 1984.

862 Gardent, M., Rabatel, A., Dedieu, J.-P., and Deline, P.: Multitemporal glacier inventory of the French Alps
863 from the late 1960s to the late 2000s, *Global and Planetary Change*, 120, 24–37,
864 <https://doi.org/10.1016/j.gloplacha.2014.05.004>, 2014.

865 Garg, P. K., Shukla, A., Tiwari, R. K., and Jasrotia, A. S.: Assessing the status of glaciers in part of the
866 Chandra basin, Himachal Himalaya: A multiparametric approach, *Geomorphology*, 284, 99–114,
867 <https://doi.org/10.1016/j.geomorph.2016.10.022>, 2017.

868 Gilbert, A. and Vincent, C.: Atmospheric temperature changes over the 20th century at very high
869 elevations in the European Alps from englacial temperatures: EUROPEAN ALPS AIR TEMPERATURE
870 CHANGES, *Geophys. Res. Lett.*, 40, 2102–2108, <https://doi.org/10.1002/grl.50401>, 2013.

871 Gruber, S. and Haeberli, W.: Permafrost in steep bedrock slopes and its temperature-related
872 destabilization following climate change, *J. Geophys. Res.*, 112, F02S18,
873 <https://doi.org/10.1029/2006JF000547>, 2007.

874 Guillet, G. and Ravel, L.: Variations in surface area of six ice aprons in the Mont-Blanc massif since the
875 Little Ice Age, *J. Glaciol.*, 66, 777–789, <https://doi.org/10.1017/jog.2020.46>, 2020.

876 Guillet, G., Preunkert, S., Ravel, L., Montagnat, M., and Friedrich, R.: Investigation of a cold-based ice
877 apron on a high-mountain permafrost rock wall using ice texture analysis and micro-¹⁴ C dating: a case
878 study of the Triangle du Tacul ice apron (Mont Blanc massif, France), *J. Glaciol.*, 1–8,
879 <https://doi.org/10.1017/jog.2021.65>, 2021.

880 Haeberli, W. and Gruber, S.: Global Warming and Mountain Permafrost, in: *Permafrost Soils*, vol. 16,
881 edited by: Margesin, R., Springer Berlin Heidelberg, Berlin, Heidelberg, 205–218,
882 https://doi.org/10.1007/978-3-540-69371-0_14, 2009.

883 Han, Y. and Oh, J.: Automated Geo/Co-Registration of Multi-Temporal Very-High-Resolution Imagery,
884 *Sensors*, 18, 1599, <https://doi.org/10.3390/s18051599>, 2018.

885 Hantel, M., Maurer, C., and Mayer, D.: The snowline climate of the Alps 1961–2010, *Theor Appl Climatol*,
886 110, 517–537, <https://doi.org/10.1007/s00704-012-0688-9>, 2012.

887 Hasler, A., Gruber, S., and Haeberli, W.: Temperature variability and thermal offset in steep alpine rock
888 and ice faces, *Frozen Ground*, <https://doi.org/10.5194/tcd-5-721-2011>, 2011.

889 Hock, R.: Temperature index melt modelling in mountain areas, *Journal of Hydrology*, 282, 104–115,
890 [https://doi.org/10.1016/S0022-1694\(03\)00257-9](https://doi.org/10.1016/S0022-1694(03)00257-9), 2003.

891 Hoelzle, M., Haeberli, W., Dischl, M., and Peschke, W.: Secular glacier mass balances derived from
892 cumulative glacier length changes, *Global and Planetary Change*, 36, 295–306,
893 [https://doi.org/10.1016/S0921-8181\(02\)00223-0](https://doi.org/10.1016/S0921-8181(02)00223-0), 2003.

894 Höhle, J. and Höhle, M.: Accuracy assessment of digital elevation models by means of robust statistical
895 methods, *ISPRS Journal of Photogrammetry and Remote Sensing*, 64, 398–406,
896 <https://doi.org/10.1016/j.isprsjprs.2009.02.003>, 2009.

897 Hoy, A., Hänsel, S., Skalak, P., Ustrnul, Z., and Bochníček, O.: The extreme European summer of 2015 in a
898 long-term perspective: EXTREME EUROPEAN SUMMER OF 2015 IN A LONG-TERM PERSPECTIVE, *Int. J.*
899 *Climatol.*, 37, 943–962, <https://doi.org/10.1002/joc.4751>, 2017.

900 Huss, M., Funk, M., and Ohmura, A.: Strong Alpine glacier melt in the 1940s due to enhanced solar
901 radiation, *Geophys. Res. Lett.*, 36, L23501, <https://doi.org/10.1029/2009GL040789>, 2009.

902 Immerzeel, W. W., Pellicciotti, F., and Bierkens, M. F. P.: Rising river flows throughout the twenty-first
 903 century in two Himalayan glacierized watersheds, *Nature Geosci*, 6, 742–745,
 904 <https://doi.org/10.1038/ngeo1896>, 2013.

905 IPCC, 2021: Climate Change 2021: The Physical Science Basis. Contribution of Working Group I to the
 906 Sixth Assessment Report of the Intergovernmental Panel on Climate Change, 2021.

907 Jiskoot, H., Curran, C. J., Tessler, D. L., and Shenton, L. R.: Changes in Clemenceau Icefield and Chaba
 908 Group glaciers, Canada, related to hypsometry, tributary detachment, length–slope and area–aspect
 909 relations, *Ann. Glaciol.*, 50, 133–143, <https://doi.org/10.3189/172756410790595796>, 2009.

910 Johnson, E. and Rupper, S.: An Examination of Physical Processes That Trigger the Albedo-Feedback on
 911 Glacier Surfaces and Implications for Regional Glacier Mass Balance Across High Mountain Asia, *Front.*
 912 *Earth Sci.*, 8, 129, <https://doi.org/10.3389/feart.2020.00129>, 2020.

913 Kaushik, S., Ravel, L., Magnin, F., Yan, Y., Trouve, E., and Cusicanqui, D.: DISTRIBUTION AND
 914 EVOLUTION OF ICE APRONS IN A CHANGING CLIMATE IN THE MONT-BLANC MASSIF (WESTERN
 915 EUROPEAN ALPS), *Int. Arch. Photogramm. Remote Sens. Spatial Inf. Sci.*, XLIII-B3-2021, 469–475,
 916 <https://doi.org/10.5194/isprs-archives-XLIII-B3-2021-469-2021>, 2021.

917 Kraaijenbrink, P. D. A., Bierkens, M. F. P., Lutz, A. F., and Immerzeel, W. W.: Impact of a global
 918 temperature rise of 1.5 degrees Celsius on Asia’s glaciers, *Nature*, 549, 257–260,
 919 <https://doi.org/10.1038/nature23878>, 2017.

920 Kuroiwa, D., Mizuno, Y., and Takeuchi, M.: Micromeritical properties of snow., *Physics of Snow and Ice*,
 921 1, 751–772, 1967.

922 Laha, S., Kumari, R., Singh, S., Mishra, A., Sharma, T., Banerjee, A., Nainwal, H. C., and Shankar, R.:
 923 Evaluating the contribution of avalanching to the mass balance of Himalayan glaciers, *Ann. Glaciol.*, 58,
 924 110–118, <https://doi.org/10.1017/aog.2017.27>, 2017.

925 Li, K., Li, H., Wang, L., and Gao, W.: On the relationship between local topography and small glacier
 926 change under climatic warming on Mt. Bogda, eastern Tian Shan, China, *J. Earth Sci.*, 22, 515–527,
 927 <https://doi.org/10.1007/s12583-011-0204-7>, 2011.

928 Liu, T., Kinouchi, T., and Ledezma, F.: Characterization of recent glacier decline in the Cordillera Real by
 929 LANDSAT, ALOS, and ASTER data, *Remote Sensing of Environment*, 137, 158–172,
 930 <https://doi.org/10.1016/j.rse.2013.06.010>, 2013.

931 Lopez, P., Chevallier, P., Favier, V., Pouyaud, B., Ordenes, F., and Oerlemans, J.: A regional view of
 932 fluctuations in glacier length in southern South America, *Global and Planetary Change*, 71, 85–108,
 933 <https://doi.org/10.1016/j.gloplacha.2009.12.009>, 2010.

934 Magnin, F., Brenning, A., Bodin, X., Deline, P., and Ravel, L.: Modélisation statistique de la distribution
 935 du permafrost de paroi : application au massif du Mont Blanc, *geomorphologie*, 21, 145–162,
 936 <https://doi.org/10.4000/geomorphologie.10965>, 2015.

937 Magnin, F., Westermann, S., Pogliotti, P., Ravel, L., Deline, P., and Malet, E.: Snow control on active
 938 layer thickness in steep alpine rock walls (Aiguille du Midi, 3842ma.s.l., Mont Blanc massif), *CATENA*,
 939 149, 648–662, <https://doi.org/10.1016/j.catena.2016.06.006>, 2017.

940 Magnin, F., Etzel Müller, B., Westermann, S., Isaksen, K., Hilger, P., and Hermanns, R. L.: Permafrost
 941 distribution in steep rock slopes in Norway: measurements, statistical modelling and implications for
 942 geomorphological processes, *Earth Surf. Dynam.*, 7, 1019–1040, [https://doi.org/10.5194/esurf-7-1019-](https://doi.org/10.5194/esurf-7-1019-2019)
 943 2019, 2019.

944 Mahmoud Sabo, L., Mariun, N., Hizam, H., Mohd Radzi, M. A., and Zakaria, A.: Estimation of solar
 945 radiation from digital elevation model in area of rough topography, *WJE*, 13, 453–460,
 946 <https://doi.org/10.1108/WJE-08-2016-0063>, 2016.

947 Marti, R., Gascoin, S., Berthier, E., de Pinel, M., Houet, T., and Laffly, D.: Mapping snow depth in open
 948 alpine terrain from stereo satellite imagery, *The Cryosphere*, 10, 1361–1380, [https://doi.org/10.5194/tc-](https://doi.org/10.5194/tc-10-1361-2016)
 949 10-1361-2016, 2016.

950 Meehl, G. A. and Tebaldi, C.: More Intense, More Frequent, and Longer Lasting Heat Waves in the 21st
 951 Century, *Science*, 305, 994–997, <https://doi.org/10.1126/science.1098704>, 2004.

952 Meier, W. J.-H., Griesinger, J., Hochreuther, P., and Braun, M. H.: An Updated Multi-Temporal Glacier
 953 Inventory for the Patagonian Andes With Changes Between the Little Ice Age and 2016, *Front. Earth Sci.*,
 954 6, 62, <https://doi.org/10.3389/feart.2018.00062>, 2018.

955 Mölg, T.: Ablation and associated energy balance of a horizontal glacier surface on Kilimanjaro, *J.*
 956 *Geophys. Res.*, 109, D16104, <https://doi.org/10.1029/2003JD004338>, 2004.

957 Mourey, J., Marcuzzi, M., Ravanel, L., and Pallandre, F.: Effects of climate change on high Alpine
 958 mountain environments: Evolution of mountaineering routes in the Mont Blanc massif (Western Alps)
 959 over half a century, *Arctic, Antarctic, and Alpine Research*, 51, 176–189,
 960 <https://doi.org/10.1080/15230430.2019.1612216>, 2019.

961 Nuth, C. and Kääb, A.: Co-registration and bias corrections of satellite elevation data sets for quantifying
 962 glacier thickness change, *The Cryosphere*, 5, 271–290, <https://doi.org/10.5194/tc-5-271-2011>, 2011.

963 Oerlemans, J. and Klok, E. J.: Energy Balance of a Glacier Surface: Analysis of Automatic Weather Station
 964 Data from the Morteratschgletscher, Switzerland, *Arctic, Antarctic, and Alpine Research*, 34, 477–485,
 965 <https://doi.org/10.1080/15230430.2002.12003519>, 2002.

966 Oerlemans, J. and Reichert, B. K.: Relating glacier mass balance to meteorological data by using a
 967 seasonal sensitivity characteristic, *J. Glaciol.*, 46, 1–6, <https://doi.org/10.3189/172756500781833269>,
 968 2000.

969 Oerlemans, J., Anderson, B., Hubbard, A., Huybrechts, P., Jóhannesson, T., Knap, W. H., Schmeits, M.,
 970 Stroeve, A. P., van de Wal, R. S. W., Wallinga, J., and Zuo, Z.: Modelling the response of glaciers to
 971 climate warming, *Climate Dynamics*, 14, 267–274, <https://doi.org/10.1007/s003820050222>, 1998.

972 Olson, M. and Rupper, S.: Impacts of topographic shading on direct solar radiation for valley glaciers in
 973 complex topography, *The Cryosphere*, 13, 29–40, <https://doi.org/10.5194/tc-13-29-2019>, 2019.

974 Pandey, P. and Venkataraman, G.: Changes in the glaciers of Chandra–Bhaga basin, Himachal Himalaya,
 975 India, between 1980 and 2010 measured using remote sensing, *International Journal of Remote Sensing*,
 976 34, 5584–5597, <https://doi.org/10.1080/01431161.2013.793464>, 2013.

977 Paul, F., Kääb, A., Maisch, M., Kellenberger, T., and Haeberli, W.: Rapid disintegration of Alpine glaciers
 978 observed with satellite data: DISINTEGRATION OF ALPINE GLACIERS, *Geophys. Res. Lett.*, 31, n/a-n/a,
 979 <https://doi.org/10.1029/2004GL020816>, 2004.

980 Paul, F., Bolch, T., Briggs, K., Kääb, A., McMillan, M., McNabb, R., Nagler, T., Nuth, C., Rastner, P., Strozzi,
 981 T., and Wuite, J.: Error sources and guidelines for quality assessment of glacier area, elevation change,
 982 and velocity products derived from satellite data in the Glaciers_cci project, *Remote Sensing of*
 983 *Environment*, 203, 256–275, <https://doi.org/10.1016/j.rse.2017.08.038>, 2017.

984 Rabatel, A., Letréguilly, A., Dedieu, J.-P., and Eckert, N.: Changes in glacier equilibrium-line altitude in the
 985 western Alps from 1984 to 2010: evaluation by remote sensing and modeling of the morpho-
 986 topographic and climate controls, *The Cryosphere*, 7, 1455–1471, [https://doi.org/10.5194/tc-7-1455-](https://doi.org/10.5194/tc-7-1455-2013)
 987 2013, 2013.

988 Racoviteanu, A. E., Arnaud, Y., Williams, M. W., and Ordoñez, J.: Decadal changes in glacier parameters
 989 in the Cordillera Blanca, Peru, derived from remote sensing, *J. Glaciol.*, 54, 499–510,
 990 <https://doi.org/10.3189/002214308785836922>, 2008.

991 Rafiq, M. and Mishra, A.: Investigating changes in Himalayan glacier in warming environment: a case
 992 study of Kolahoi glacier, *Environ Earth Sci*, 75, 1469, <https://doi.org/10.1007/s12665-016-6282-1>, 2016.

993 Rastner, P., Prinz, R., Notarnicola, C., Nicholson, L., Sailer, R., Schwaizer, G., and Paul, F.: On the
 994 Automated Mapping of Snow Cover on Glaciers and Calculation of Snow Line Altitudes from Multi-
 995 Temporal Landsat Data, *Remote Sensing*, 11, 1410, <https://doi.org/10.3390/rs11121410>, 2019.

996 Ravanel, L., Deline, P., Lambiel, C., and Vincent, C.: Instability of a high alpine rock ridge: the lower arête
 997 des cosmiques, mont blanc massif, france, *Geografiska Annaler: Series A, Physical Geography*, 95, 51–66,
 998 <https://doi.org/10.1111/geoa.12000>, 2013.

999 Ravanel, L., Duvillard, P., Jaboyedoff, M., and Lambiel, C.: Recent evolution of an ice-cored moraine at
 1000 the G entianes P ass, V alais A lps, S witzerland, *Land Degrad. Develop.*, 29, 3693–3708,
 1001 <https://doi.org/10.1002/ldr.3088>, 2018.

1002 Salerno, F., Thakuri, S., Tartari, G., Nuimura, T., Sunako, S., Sakai, A., and Fujita, K.: Debris-covered
 1003 glacier anomaly? Morphological factors controlling changes in the mass balance, surface area, terminus
 1004 position, and snow line altitude of Himalayan glaciers, *Earth and Planetary Science Letters*, 471, 19–31,
 1005 <https://doi.org/10.1016/j.epsl.2017.04.039>, 2017.

1006 Sappington, J. M., Longshore, K. M., and Thompson, D. B.: Quantifying Landscape Ruggedness for Animal
 1007 Habitat Analysis: A Case Study Using Bighorn Sheep in the Mojave Desert, *Journal of Wildlife*
 1008 *Management*, 71, 1419–1426, <https://doi.org/10.2193/2005-723>, 2007.

1009 Scherler, D., Bookhagen, B., and Strecker, M. R.: Spatially variable response of Himalayan glaciers to
 1010 climate change affected by debris cover, *Nature Geosci.*, 4, 156–159, <https://doi.org/10.1038/ngeo1068>,
 1011 2011.

1012 Schweizer, J.: Snow avalanche formation, *Rev. Geophys.*, 41, 1016,
 1013 <https://doi.org/10.1029/2002RG000123>, 2003.

1014 Serquet, G., Marty, C., Dulex, J.-P., and Rebetez, M.: Seasonal trends and temperature dependence of
 1015 the snowfall/precipitation-day ratio in Switzerland: SNOWFALL/PRECIPITATION-DAY RATIO, *Geophys.*
 1016 *Res. Lett.*, 38, n/a-n/a, <https://doi.org/10.1029/2011GL046976>, 2011.

1017 Shean, D. E., Alexandrov, O., Moratto, Z. M., Smith, B. E., Joughin, I. R., Porter, C., and Morin, P.: An
 1018 automated, open-source pipeline for mass production of digital elevation models (DEMs) from very-
 1019 high-resolution commercial stereo satellite imagery, *ISPRS Journal of Photogrammetry and Remote*
 1020 *Sensing*, 116, 101–117, <https://doi.org/10.1016/j.isprsjprs.2016.03.012>, 2016.

1021 Shukla, A. and Qadir, J.: Differential response of glaciers with varying debris cover extent: evidence from
 1022 changing glacier parameters, *International Journal of Remote Sensing*, 37, 2453–2479,
 1023 <https://doi.org/10.1080/01431161.2016.1176272>, 2016.

1024 Singh, V. P., Singh, P., and Haritashya, U. K.: *Encyclopedia of snow, ice and glaciers*, Springer, Dordrecht
 1025 London, 2011.

1026 Smith, C. D.: The Relationship between Monthly Precipitation and Elevation in the Alberta Foothills
 1027 during the Foothills Orographic Precipitation Experiment, in: *Cold Region Atmospheric and Hydrologic*
 1028 *Studies. The Mackenzie GEWEX Experience*, edited by: Woo, M., Springer Berlin Heidelberg, Berlin,
 1029 Heidelberg, 167–185, https://doi.org/10.1007/978-3-540-73936-4_10, 2008.

1030 Sorg, A., Huss, M., Rohrer, M., and Stoffel, M.: The days of plenty might soon be over in glacierized
 1031 Central Asian catchments, *Environ. Res. Lett.*, 9, 104018, [https://doi.org/10.1088/1748-](https://doi.org/10.1088/1748-9326/9/10/104018)
 1032 [9326/9/10/104018](https://doi.org/10.1088/1748-9326/9/10/104018), 2014.

1033 Tangborn, W. V., Fountain, A. G., and Sikonia, W. G.: Effect of Area Distribution with Altitude on Glacier
 1034 Mass Balance – A Comparison of North and South Klawatti Glaciers, Washington State, U.S.A., *A.*
 1035 *Glaciology.*, 14, 278–282, <https://doi.org/10.1017/S0260305500008752>, 1990.

1036 Thibert, E., Dkengne Sielenou, P., Vionnet, V., Eckert, N., and Vincent, C.: Causes of Glacier Melt
 1037 Extremes in the Alps Since 1949, *Geophys. Res. Lett.*, 45, 817–825,
 1038 <https://doi.org/10.1002/2017GL076333>, 2018.

1039 Triglav-Čekada, M. and Gabrovec, M.: Documentation of Triglav glacier, Slovenia, using non-metric
 1040 panoramic images, *Ann. Glaciol.*, 54, 80–86, <https://doi.org/10.3189/2013AoG62A095>, 2013.

1041 Vernay, M., Lafaysse, M., Hagenmuller, P., Nheili, R., Verfaillie, D., and Morin, S.: The S2M
 1042 meteorological and snow cover reanalysis in the French mountainous areas (1958 - present),
 1043 <https://doi.org/10.25326/37>, 2019.

1044 Vincent, C.: Influence of climate change over the 20th Century on four French glacier mass balances, *J.*
 1045 *Geophys. Res.*, 107, 4375, <https://doi.org/10.1029/2001JD000832>, 2002.

1046 Vincent, C. and Vallon, M.: Meteorological controls on glacier mass balance: empirical relations
 1047 suggested by measurements on glacier de Sarennes, France, *J. Glaciol.*, 43, 131–137,
 1048 <https://doi.org/10.3189/S0022143000002896>, 1997.

1049 Vionnet, V., Brun, E., Morin, S., Boone, A., Faroux, S., Le Moigne, P., Martin, E., and Willemet, J.-M.: The
 1050 detailed snowpack scheme Crocus and its implementation in SURFEX v7.2, *Geosci. Model Dev.*, 5, 773–
 1051 791, <https://doi.org/10.5194/gmd-5-773-2012>, 2012.

Warren, C. R.: Terminal environment, topographic control and fluctuations of West Greenland glaciers, *Boreas*, 20, 1–15, <https://doi.org/10.1111/j.1502-3885.1991.tb00453.x>, 2008.

Yalcin, M.: The impact of topographical parameters to the glaciation and glacial retreat on Mount Ağı (Ararat), *Environ Earth Sci*, 78, 393, <https://doi.org/10.1007/s12665-019-8374-1>, 2019.

Yang, M., Wang, X., Pang, G., Wan, G., and Liu, Z.: The Tibetan Plateau cryosphere: Observations and model simulations for current status and recent changes, *Earth-Science Reviews*, 190, 353–369, <https://doi.org/10.1016/j.earscirev.2018.12.018>, 2019.

Yanuarsyah, I. and Khairiah, R. N.: Preliminary Detection Model of Rapid Mapping Technique for Landslide Susceptibility Zone Using Multi Sensor Imagery (Case Study in Banjarnegara Regency), *IOP Conf. Ser.: Earth Environ. Sci.*, 54, 012106, <https://doi.org/10.1088/1755-1315/54/1/012106>, 2017.

Tables:

Data type	Source	Resolution (m/time)	Acquisition time/period
Optical	Orthoimages IGN	0.2	July 2015
	Pleiades 1A PAN	0.5	25/08/2019, 19/08/2012
	Sentinel 2	10	12/09/2019
	SPOT 6	2.2	14/09/2019
	Pleiades 1A XS	2	19/08/2012
	Orthoimages IGN	0.5	July 2001
	Orthoimages IGN	0.5	1952
Meteorological	Col du Grand-Saint Bernard weather station (2469 m a.s.l.)	daily	1952 - 2019
	Aiguille du Midi weather station (3840 m a.s.l.)	daily	2007-2018
	SAFRAN reanalysis	daily	1958 - 2019

Table 1: Datasets used for the study.

Time period	Slope	Intercept	R ²	Pearson's r	RMSE (km ²)	p value
1952 - 2001	0.79	0.12	0.53	0.73	0.010	< 0.001
2001 - 2012	0.70	0.26	0.56	0.75	0.102	< 0.001
2012 - 2019	0.89	0.04	0.63	0.80	0.097	< 0.001

(a)

Time period	Slope	Intercept	R ²	Pearson's r	RMSE (km ²)	p value
1952 - 2001	1.01	-0.04	0.73	0.86	0.075	< 0.001

2001 - 2012	0.74	0.22	0.67	0.82	0.086	< 0.001
2012 - 2019	1.37	-0.39	0.83	0.91	0.071	< 0.001

(b)

Table 2: Linear regression parameters and correlation metrics for each period (a) using GSB transformed data and (b) using the SAFRAN reanalysis product.

Variable	Time-period	R²	Pearson's r
Direct Solar Radiation	1952 - 2001	0.64	0.79
	2001 - 2012	0.67	0.81
	2012 - 2019	0.51	0.72
Elevation	1952 - 2001	0.61	-0.78
	2001 - 2012	0.57	-0.75
	2012 - 2019	0.51	-0.71
MARST	1952 - 2001	0.40	0.63
	2001 - 2012	0.34	0.58
	2012 - 2019	0.27	0.52
TRI	1952 - 2001	0.37	0.60
	2001 - 2012	0.30	0.55
	2012 - 2019	0.32	0.57
Slope	1952 - 2001	0.29	0.54
	2001 - 2012	0.25	0.50
	2012 - 2019	0.21	0.46
Curvature	1952 - 2001	0.06	-0.26
	2001 - 2012	0.03	-0.18
	2012 - 2019	0.06	-0.24
Size of IA	1952 - 2001	0.04	-0.22
	2001 - 2012	0.06	-0.26
	2012 - 2019	0.04	-0.22

Table 3: Linear regression parameters and correlation metrics for each studied parameter.

Figures:

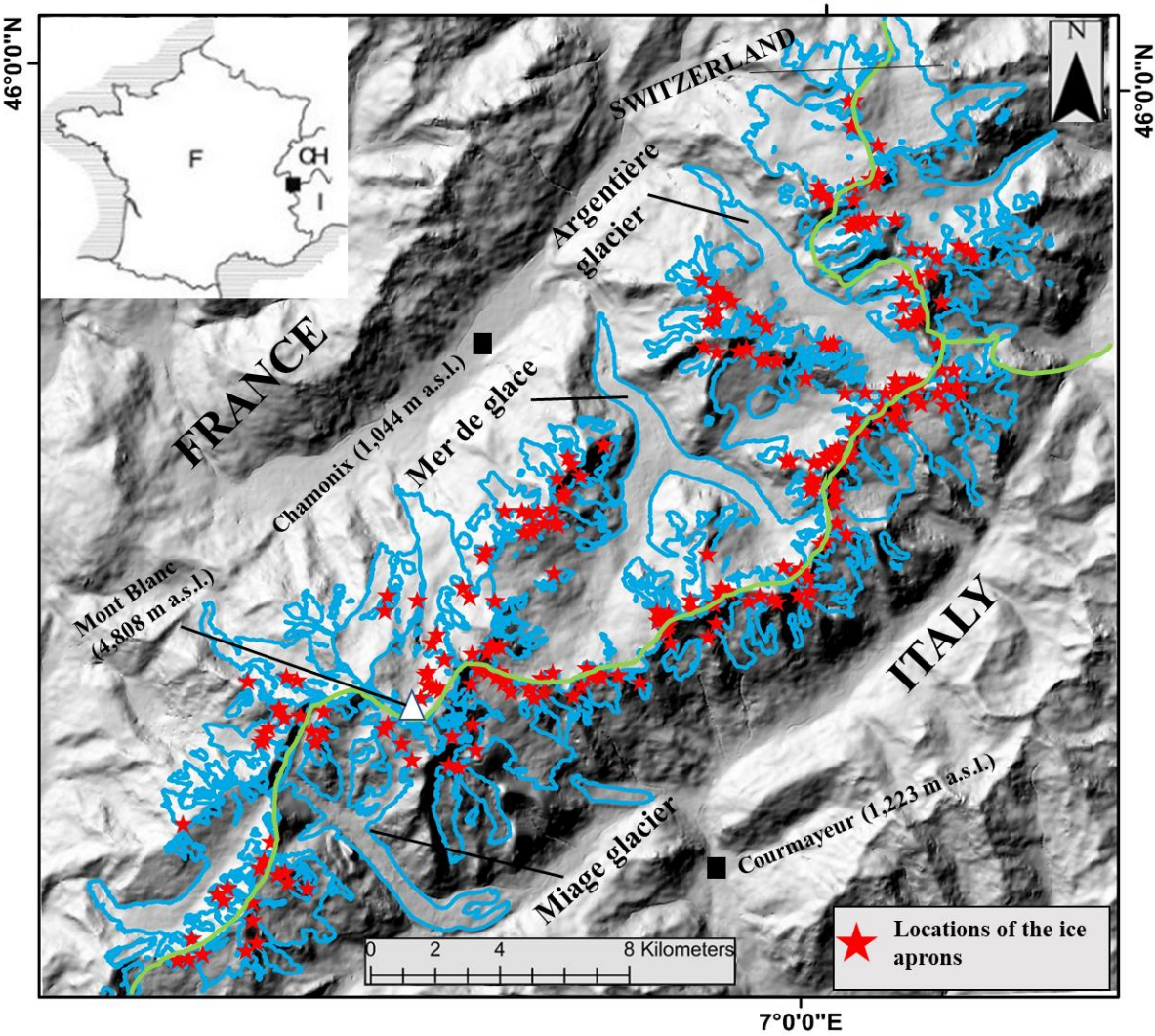


Figure 1: The Mont-Blanc massif (Western European Alps). 200 IAs (red stars) were digitized accurately on high-resolution images. The glacier outlines (in blue) comes from Gardent et al., 2014.

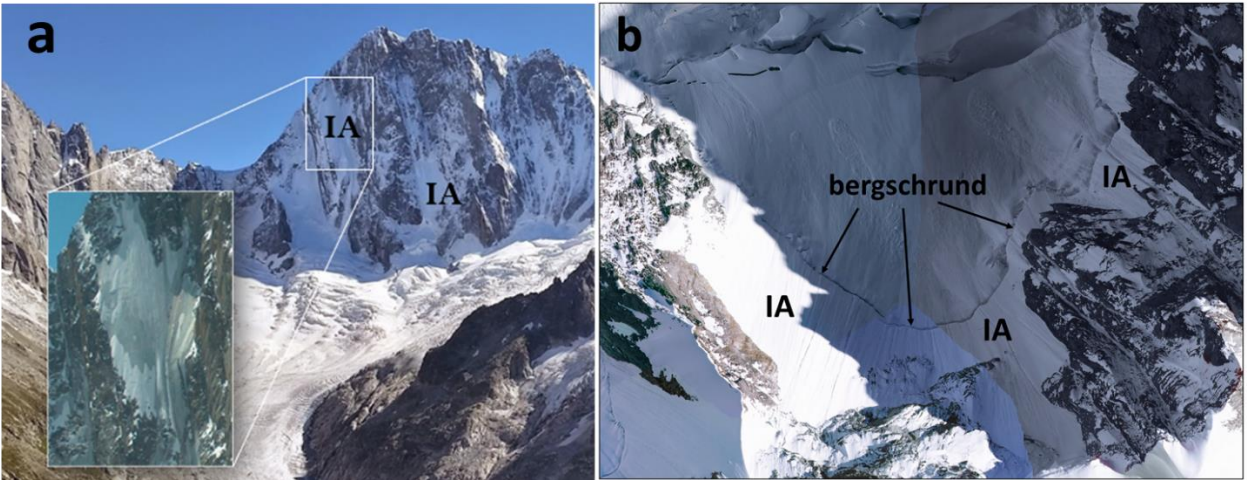


Figure 2: Ice aprons and their locations in the MBM, a. IAs on the N face of Grandes Jorasses (4208 m a.s.l.) and b. IAs on the headwall of the Argentière glacier separated by a bergschrund (3280 m a.s.l.).

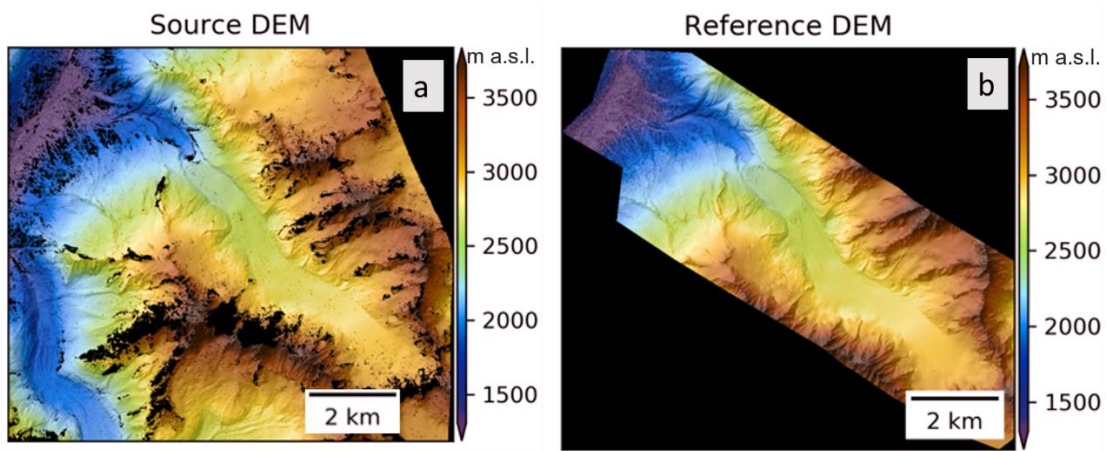


Figure 3: (a) The reference LiDAR DEM of the Argentière glacier used for co-registration, (b) the source Pleiades DEM used for further analysis.

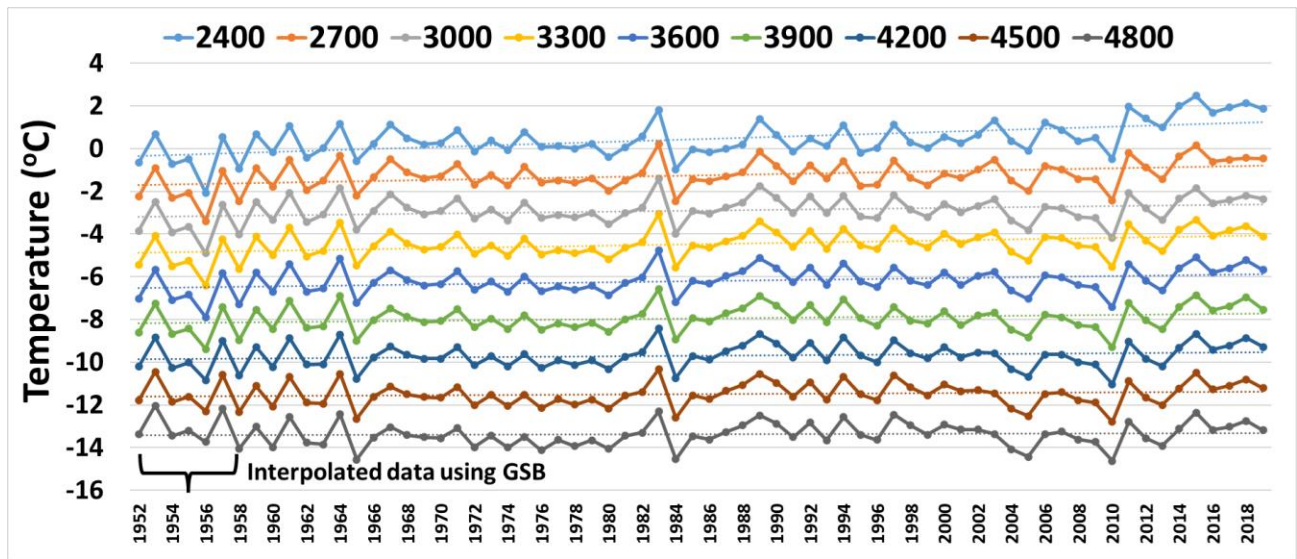


Figure 4: SAFRAN reanalysis product temperature time-series from 1952-2019 for different elevations in the MBM. The figure shows the variation of the mean annual temperatures for the entire study period.

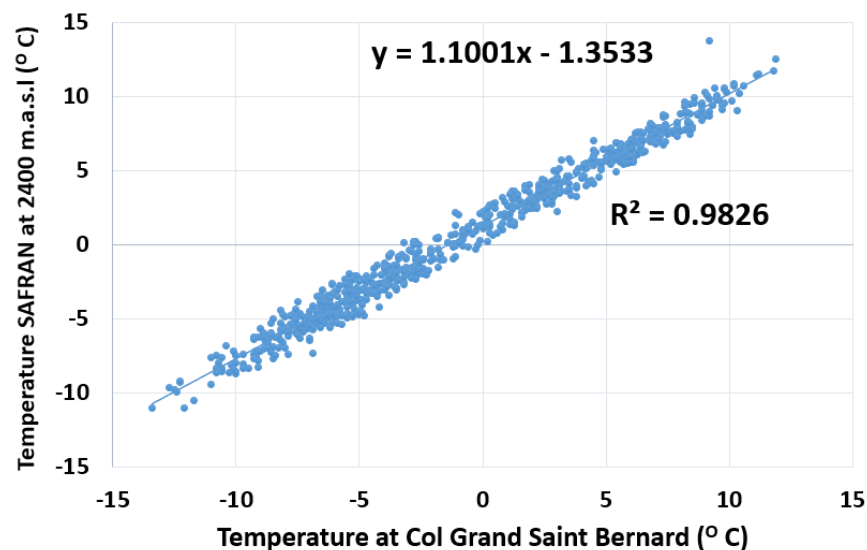


Figure 5: Correlation between the monthly averaged temperature measurements at the Col du Grand Saint Bernard (GSB) and the SAFRAN reanalysis data at 2400 m a.s.l.

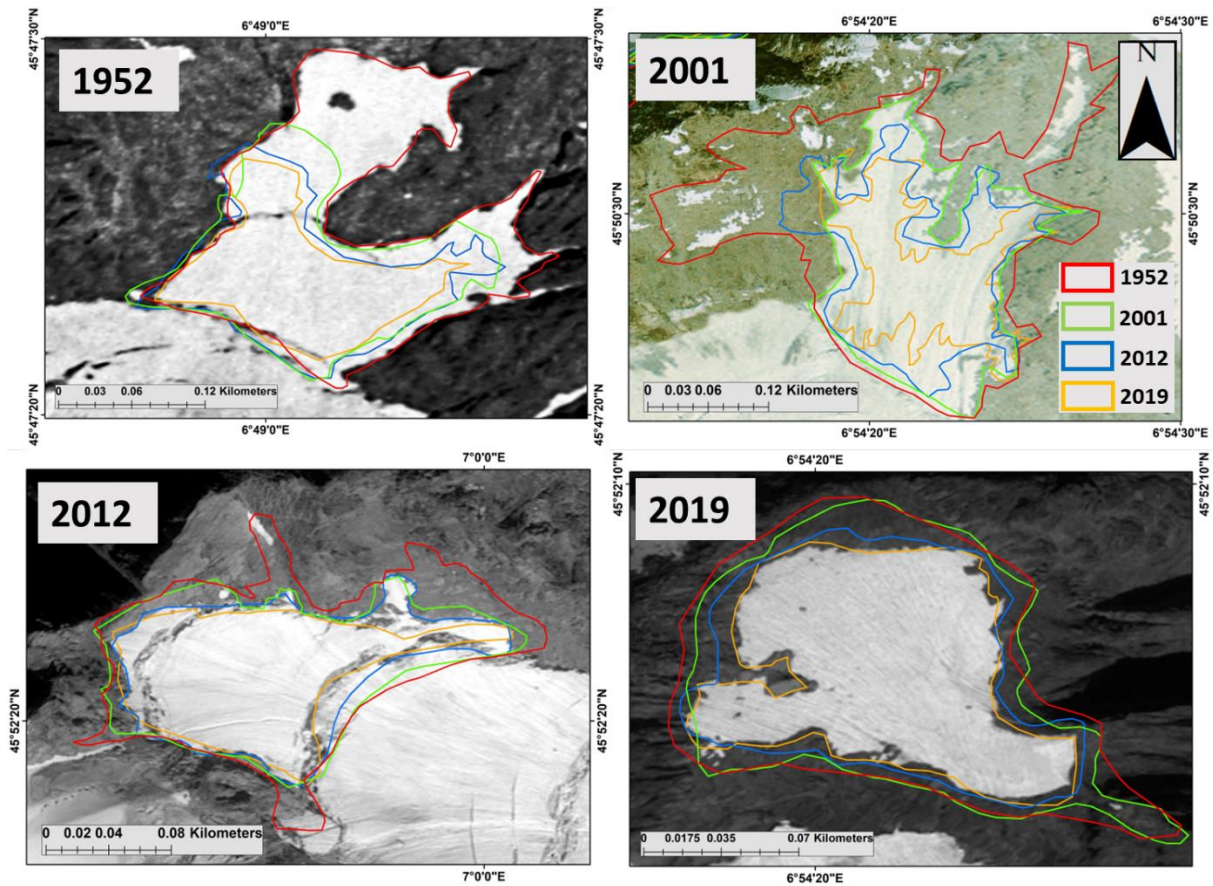
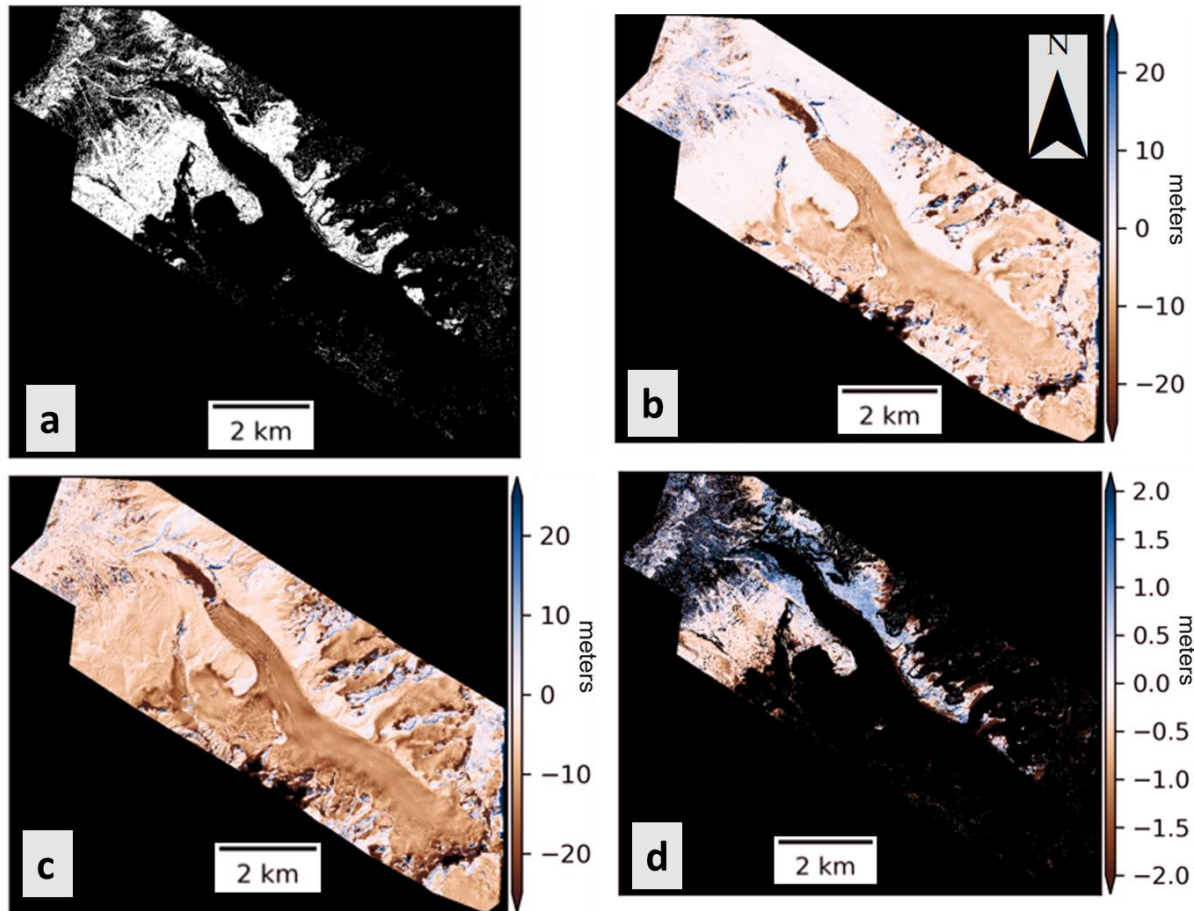


Figure 6: IAs extent delineated on high-resolution images: (a) orthophotos 1952, (b) orthophotos 2001, (c) Pleiades panchromatic 2012, (d) Pleiades panchromatic 2019. The different colour polygons represent the surface area for each date.



1130

1131 Figure 7: Stepwise Pleiades DEM accuracy assessment (a) the surfaces used for coregistration
 1132 (b) elevation difference before coregistration (c) elevation difference after coregistration
 1133 considering all areas (d) elevation difference after coregistration considering only the stable
 1134 areas.

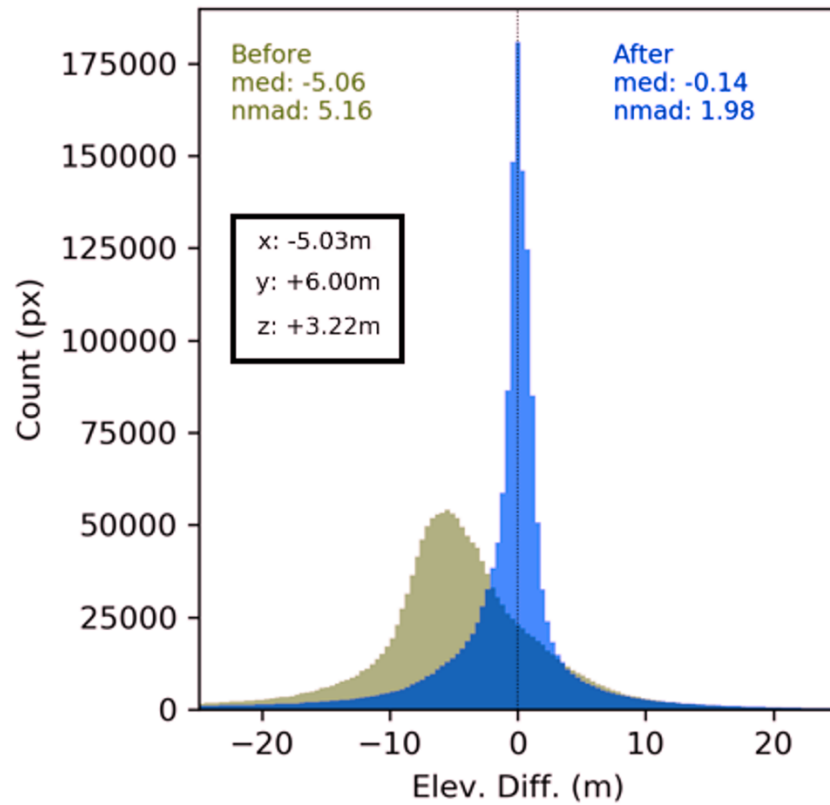


Figure 8: DEM Error (elevation difference between the reference and source DEM) distribution for stable areas

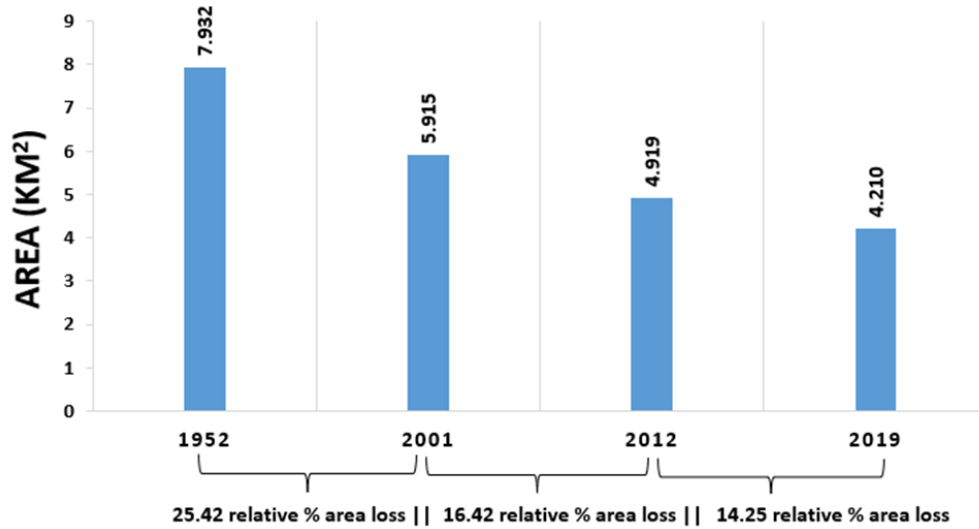
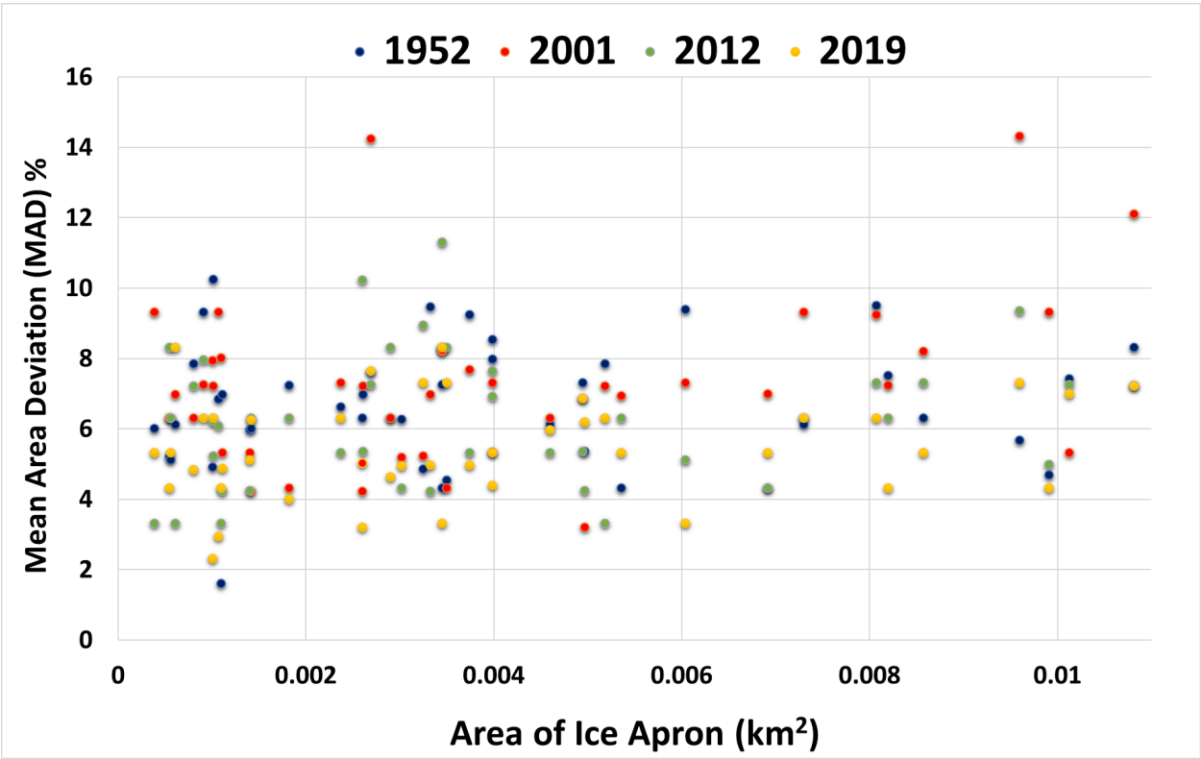


Figure 9: A comparison of the total surface area of all IAs (423 IAs) in the MBM over 67 years.

1143



1144

1145 Figure 10: The distribution of MAD values based on multiple digitizations of the IAs area for all
1146 periods.

1147

1148

1149

1150

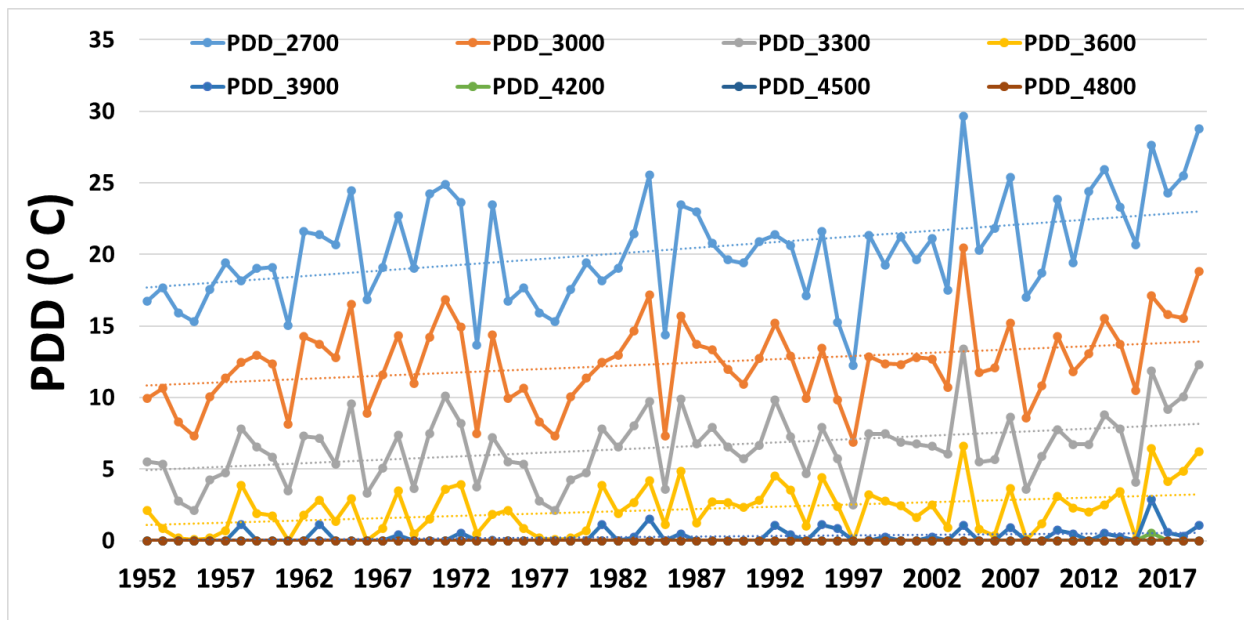


Figure 11: The variation of annual PDD values estimated based on monthly mean temperatures at different elevations in the MBM from 1952 to 2019.

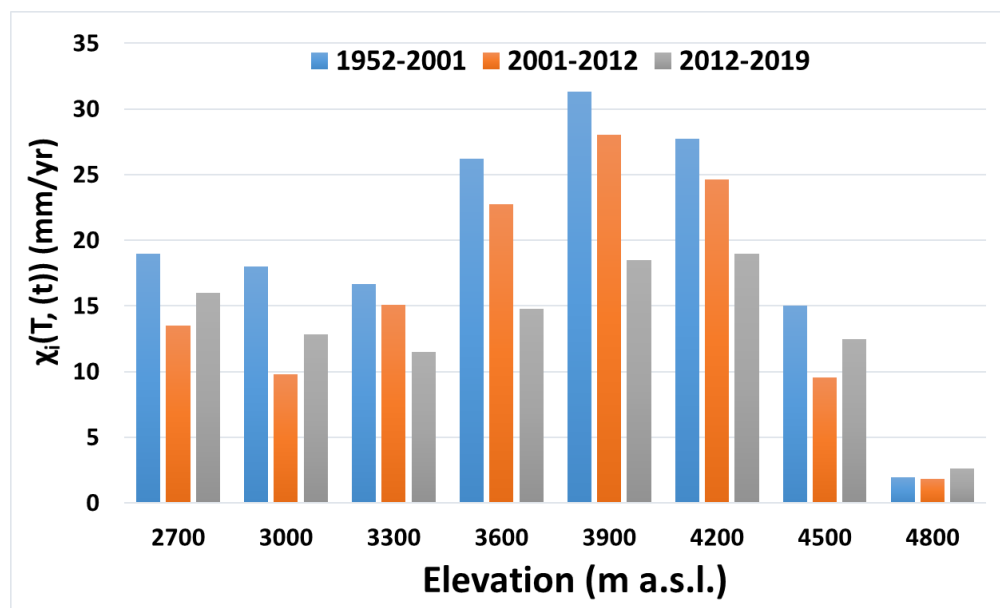


Figure 12: Variation of the average accumulation rates on steep slopes at different elevations for each period of observation

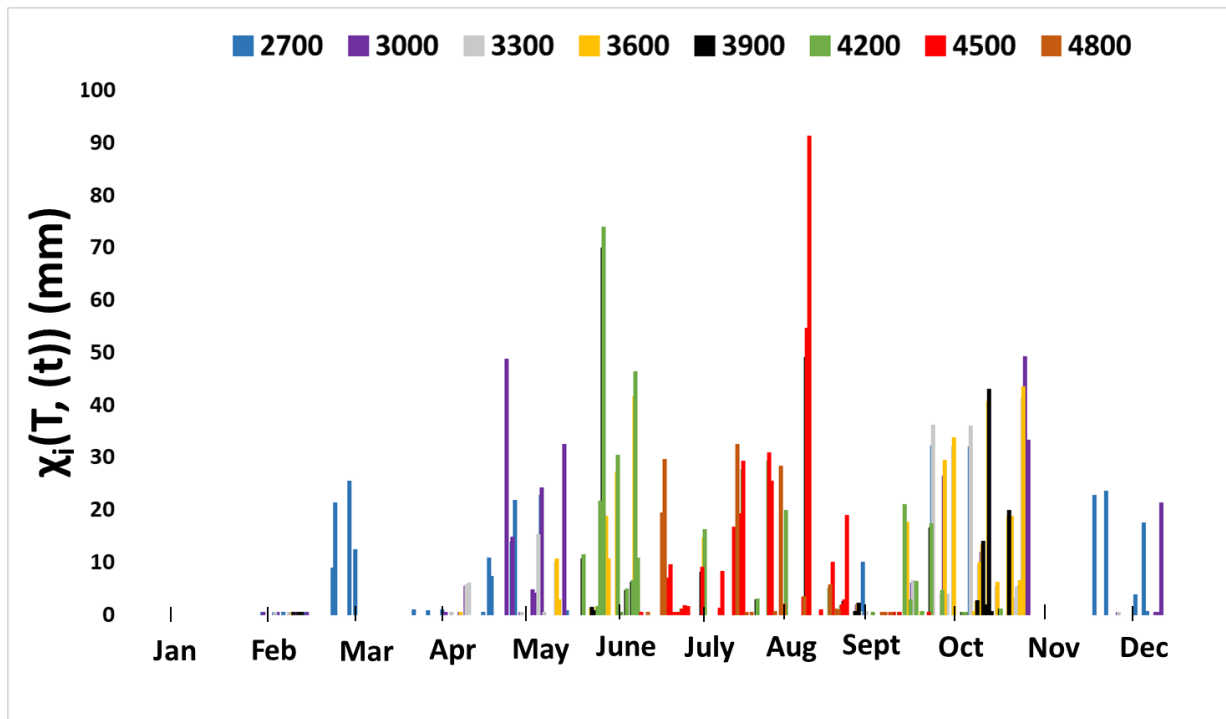


Figure 13: Accumulation (steep slopes) trends for the year 2019 at different elevations

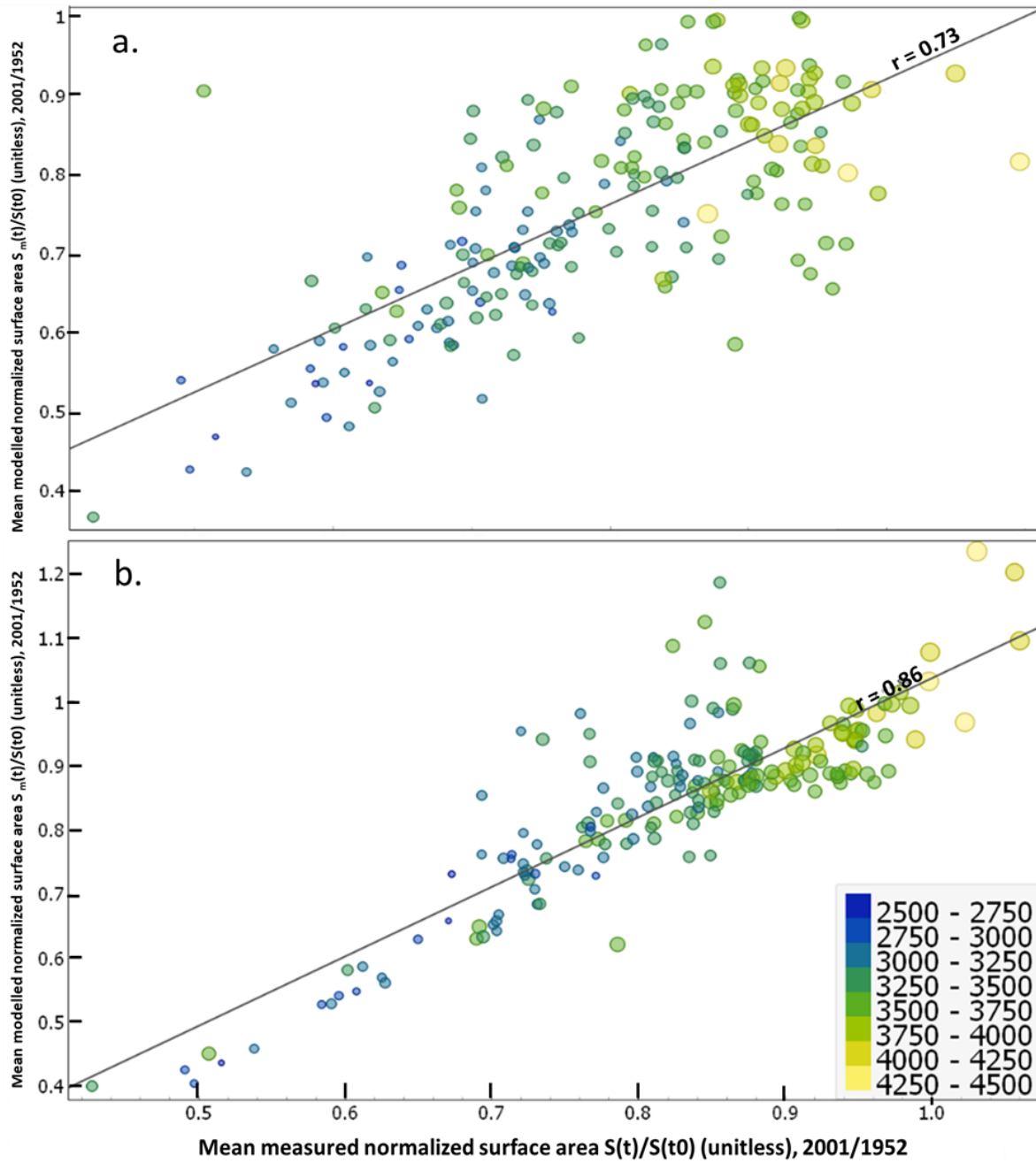


Figure 14: Correlation between the mean normalized measured and modelled surface areas (a) with GSB data transformed to AdM data and (b) with SAFRAN reanalysis data at time t . The colour and size of the ticks represent the mean elevation of the IA.

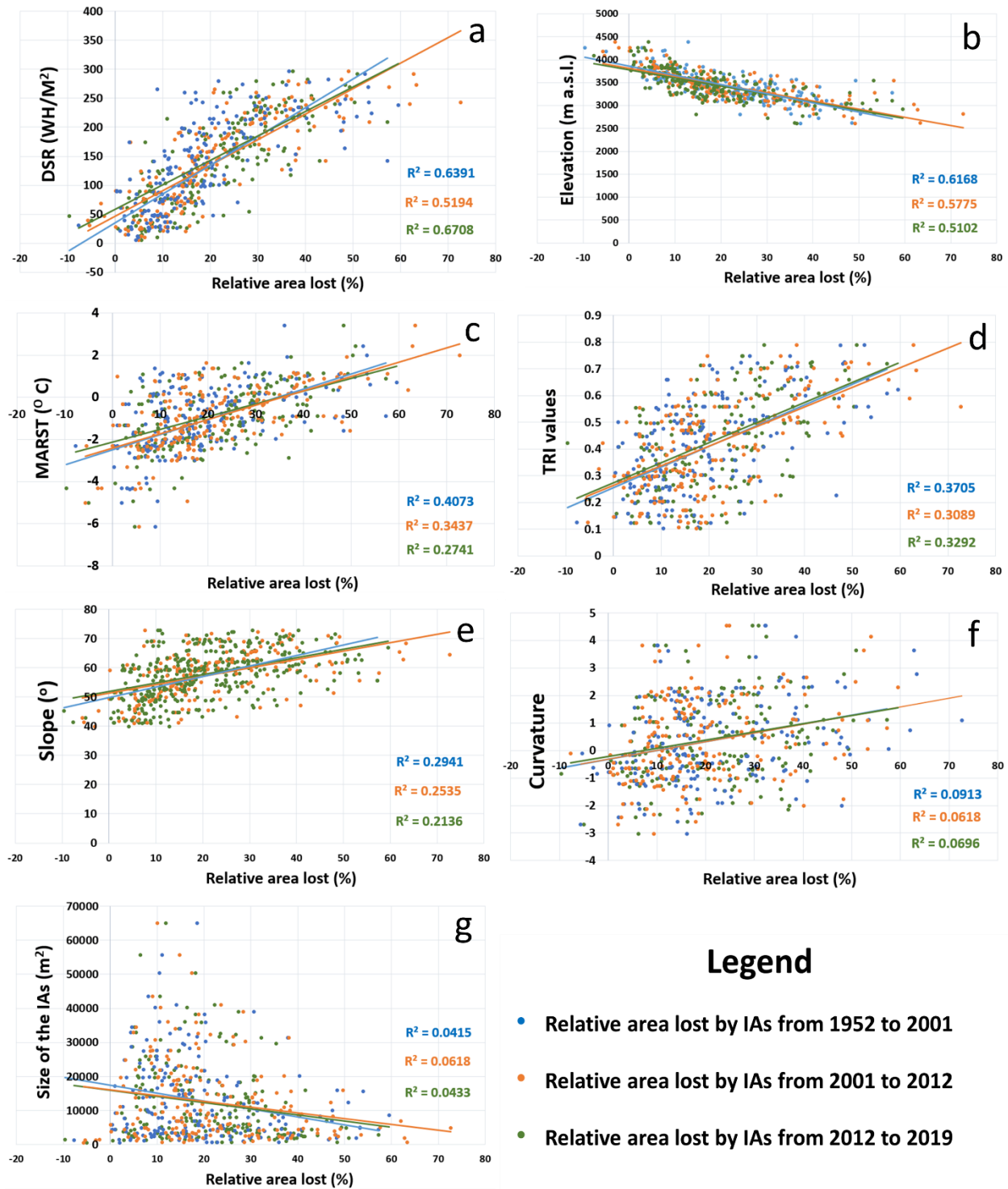
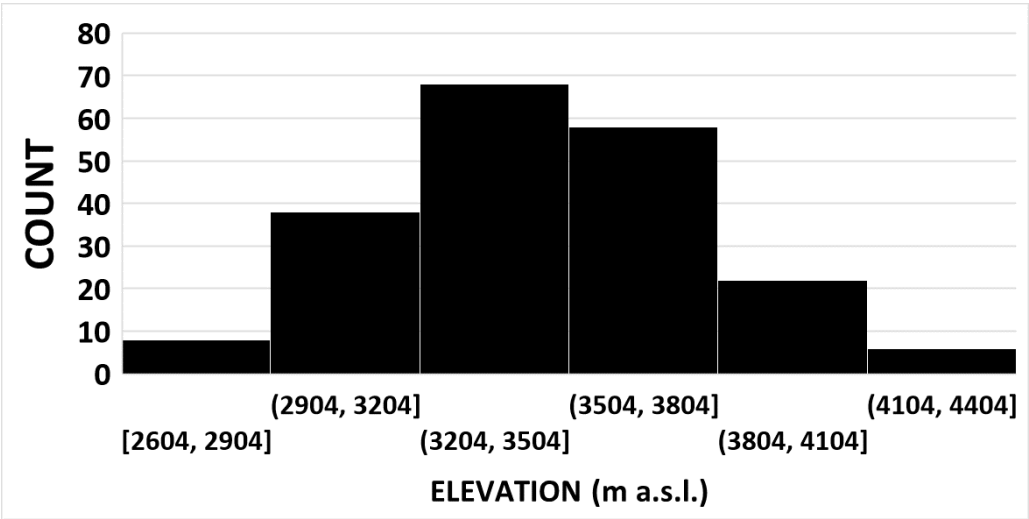


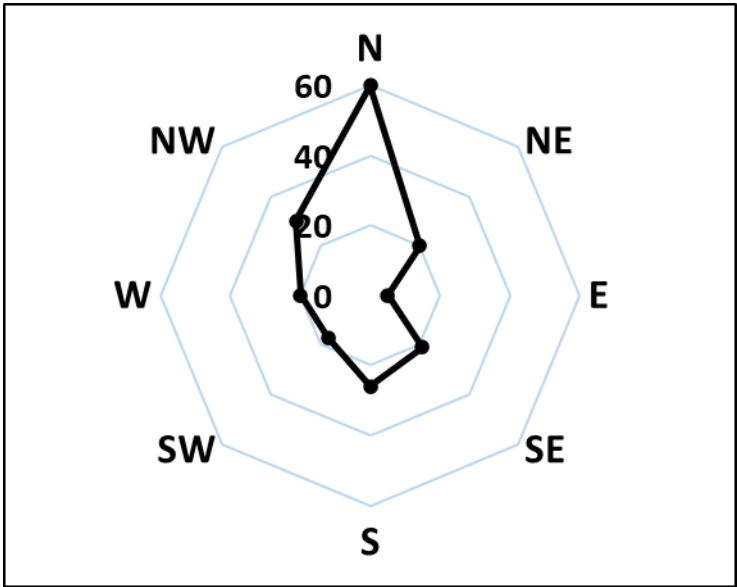
Figure 15: Scatter plots showing relationships between topographic factors and the area loss of IAs from 1952 to 2019. a) Direct solar radiation, b) elevation, c) MARST, d) TRI, e) slope, f) curvature and g) size of the IAs.

1173 Supplementary material:
1174



1175
1176 Figure 2 a: Distribution of ice aprons with elevation

1177



1178
1179 Figure 2 b: Distribution of ice aprons with the aspect

1180